Measurement of the photon detection inefficiency due to photo-nuclear interaction

Ken Sakashita
High Energy Physics Group
Department of Physics at Osaka University

April 24, 2002

Abstract

We measured the inefficiency due to photo–nuclear interaction for the CsI detector and the lead/scintillator detector. For photons with the energy, $1.5 < E_\gamma < 2.4$ GeV, the inefficiencies were $(2.93 \pm 0.89_{(stat.)}{}^{+1.15}_{-0.44}{}_{(sys.)}) \times 10^{-7}$ for CsI detector, and $(8.3 \pm 1.7_{(stat.)}{}^{+13.5}_{-1.2}{}_{(sys.)}) \times 10^{-7}$ for lead/scintillator with 6.1 X_0. The threshold is equivalent to 10 MeV incident photon energy.

We also found that the inefficiency due to photo–nuclear interaction dominates comparing to the inefficiency due to electro–magnetic interaction at $E_\gamma \sim 1.5$ GeV.

These inefficiencies are small enough to be used in the $K_L \to \pi^0 \nu \bar{\nu}$ experiment with $P_K \sim 10$ GeV.

Acknowledgement

My first thanks go to Yorikiyo Nagashima, my advisor, for giving me a wonderful opportunity for the research of high energy physics, and for his gentle support. I would like to thank M.Takita, M.Hazumi and T.Hana for their invaluable advice on physics and experimental technique.

The work presented here is the result of the efforts of many people. I would like to thank T.Nakano, Y.Sugaya, T.Yorita and LEPS collaborator. In particular, I would like to thank Y.Sugaya. He gave me many advice about DAQ system, experimental technique and more.

My special thanks go to K.Kotera, Y.Ikemoto, T.Ikei and T.Oba, who gave me invaluable advice as members of this experiment. I enjoyed having many chats with them in my research life. With M.Matsumoto and T.Ishikawa, they are KTeV group members in Osaka, I shared good time on talking about physics and lead enjoyable research life.

I also owe a lot to the members of the Yamanaka Taku Group at Osaka University for the good companionship and encouragement, K.Sumisawa, M.Yoshida, J.Ryuko, T.Houjo, K.Nitta, H.Miyake, K.Hara, Y.Kajiyama, H.Tagomori, A.Ofuji, K.Hashimoto, Y.Tamai, and B.Takeshita, have given me great deal of help proceed my research. I would like to thanks go to S.Tsuzuki and N.Sugimoto. Theirs help and support for my reserch life must also be mentioned here.

Finally, I would like to thank Taku Yamanaka. He taught me physics, experimental technique, analysis and more. I am sure this thesis did not exist without his help and advice. Even my interest in high energy physics may come from him. I had a wonderful time with him and enjoyed a lot of talks about not only physics but also natural science, computer, and life.

Contents

List of Figures

List of Tables

Chapter 1

Introduction

The existence of symmetry principles in physics had been speculated as a manifestation of underlying beauty of order of the universe. From Newtonian mechanics to quantum mechanics, symmetry principles, connected with conservation laws, have provided us economical but elegant ways of looking at the nature. The law of right-left symmetry, associated with parity conservation, and invariance in charge conjugation operation, the two discrete symmetry laws which gained importance in quantum mechanics, had also been assumed to hold in subatomic world of physics. In this context, the breakdown of the combination of charge and parity symmetry in kaon decay, following parity violation discovered in weak interactions, had given us great impact on our view of the nature. At the same time, however, the discovery opened our eyes toward a new framework of physics. Afterwards, efforts have been paid to establish a model which incorporates the CP violation.

After about three decades since the CP breaking observation, so called the Standard Model has become believed to be the most probable candidate for the full description of elementary particle physics. Recent attention has been focused upon the complete determination of the parameters introduced in this scheme. In this respect, the rare kaon decay, $K_L \to \pi^0 \nu\bar{\nu}$, has gained a key role for the determination of the parameters. We will observe the underlying physics and the purpose and overview of this study in this chapter.

1.1 Physics Interest in $K_L \to \pi^0 \nu\bar{\nu}$

1.1.1 CP Violation

The combination of charge conjugation and parity transformation changes K^0 into $\bar{K}^0$, and vice versa:

$$CP|K^0\rangle = |\bar{K^0}\rangle \, , \tag{1.1}$$

$$CP|\bar{K^0}\rangle = |K^0\rangle \, . \tag{1.2}$$

(We use a conventional phase definition, and currently neglect the small effect of CP violation.)

The eigenvalues and eigenstates of CP are described as:

$$|K_1\rangle = \frac{1}{\sqrt{2}}\left[|K^0\rangle + |\bar{K^0}\rangle\right] \qquad (CP = +1) \, , \tag{1.3}$$

$$|K_2\rangle = \frac{1}{\sqrt{2}}\left[|K^0\rangle - |\bar{K^0}\rangle\right] \qquad (CP = -1) \, . \tag{1.4}$$

K_2 is the longer-lived kaons, whose lifetime is 5.2×10^{-8} seconds, and K_1 is the shorter-lived kaons, whose lifetime is 0.89×10^{-10} seconds. It had been believed from CP consistency that $|K_2\rangle$ decays to the three pions, which form a CP odd state, while $|K_1\rangle$ decays to two pions in a CP even state.

In 1964, Cronin and Fitch, *et al.*, observed that the longer-lived kaons decayed to two pions [1]. This suggests that CP odd long-lived kaons, K_L, decays into CP even mode, and CP is not conserved in this decay.

This phenomenon can be explained if K_L is actually composed not only of $|K_2\rangle$ but also with a slight mixture of $|K_1\rangle$:

$$|K_L\rangle = \frac{1}{\sqrt{1+\epsilon^2}}\left[|K_2\rangle + \epsilon|K_1\rangle\right] , \tag{1.5}$$

and K_1 decays to two pions. Such a mechanism for causing K_L to decay to two pions is called indirect CP violation. However, CP can be violated if K_2 in equation (1.5) decays to two π^0's. If K_2 directly decays to two pions, we can say that the CP is directly violated.

1.1.2 CKM parameter η

Currently, the powerful framework to explain CP violation is the Standard Model, which incorporates electromagnetic, weak, and strong interactions into a single scheme. It has a mechanism to introduce CP violation, including the direct CP violation.

In the Standard Model picture, direct CP violation is connected to the framework of quark mixing presented by Cabbibo, Koboyashi, and Maskawa [2]. In this theory, direct CP violation stems from the consequence of a three generation model.

The charged current in weak interaction can be written as:

$$J^\mu = \begin{pmatrix} \bar{u} & \bar{c} & \bar{t} \end{pmatrix} \frac{\gamma^\mu(1-\gamma^5)}{2} U \begin{pmatrix} d \\ s \\ b \end{pmatrix} . \tag{1.6}$$

The matrix U, introduced by Kobayashi and Maskawa, tells us the coupling of up and down type quarks:

$$U = \begin{pmatrix} V_{ud} & V_{us} & V_{ub} \\ V_{cd} & V_{cs} & V_{cb} \\ V_{td} & V_{ts} & V_{tb} \end{pmatrix} . \tag{1.7}$$

The 3×3 unitary matrix U can be represented by 4 parameters, with 5 arbitrary phases left aside. Of 4 parameters, 3 are real parameters and 1 is complex phase factor which accounts for the CP violation.

Wolfenstein parameterized the matrix components as follows [3]:

$$U = \begin{pmatrix} 1-\frac{\lambda^2}{2} & \lambda & A\lambda^3(\rho - i\eta) \\ -\lambda & 1-\frac{\lambda^2}{2} & A\lambda^2 \\ A\lambda^3(1-\rho-i\eta) & -A\lambda^2 & 1 \end{pmatrix} . \tag{1.8}$$

The η parameter accounts for the CP violation, and the determination of the η parameter is one of the primary goals of particle physics of today. As we will see, measurement of the branching ratio of rare CP violating decays can determine the value of η.

1.1.3 Decay of $K_L \to \pi^0 \nu\bar{\nu}$

The observation of a rare decay $K_L \to \pi^0 \nu\bar{\nu}$ is a good window to determine the η parameter. As shown in Fig. 1.1, this decay is governed by short-distance transition current and occurs almost entirely from the direct CP violation, as described below.

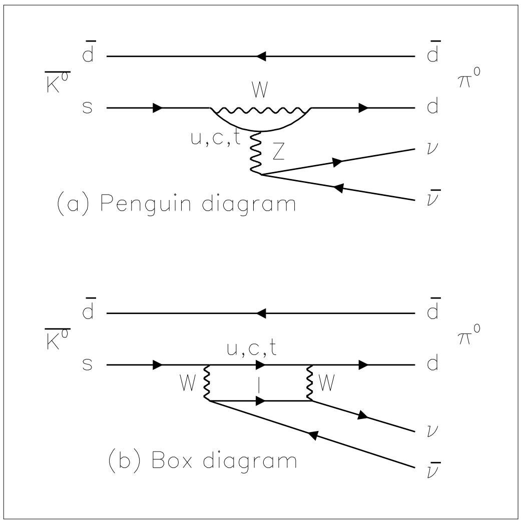

Figure 1.1: The Z penguin and W-box diagrams which contributeto the decay $K_L \to \pi^0 \nu\bar{\nu}$

The amplitude for $K_L \to \pi^0 \nu\bar{\nu}$ can be written as

$$A(K_L \to \pi^0 \nu\bar{\nu}) = \frac{1}{\sqrt{1+\epsilon^2}} \left[A(K_2 \to \pi^0 \nu\bar{\nu}) + \epsilon A(K_1 \to \pi^0 \nu\bar{\nu}) \right] , \tag{1.9}$$

or

$$A(K_L \to \pi^0 \nu\bar{\nu}) = \frac{1}{\sqrt{2(1+\epsilon^2)}} \left[(1+\epsilon) A(K^0 \to \pi^0 \nu\bar{\nu}) - (1-\epsilon) A(\bar{K^0} \to \pi^0 \nu\bar{\nu}) \right] , \tag{1.10}$$

using equations (1.3) and (1.4). Since top quark can be in medium state(Fig. 1.1), this decay involves to the V_{td} and V_{ts}. Using the Wolfenstein's parameterization (1.8),

$$A(K_L \to \pi^0 \nu\bar{\nu}) \propto V_{td}^* V_{ts} - V_{ts}^* V_{td} \sim 2i\eta \, . \tag{1.11}$$

Thus, we can see that the branching ratio of $K_L \to \pi^0 \nu\bar{\nu}$ is proportional to η^2, and determines the η parameter.

The branching ratio can be calculated [4, 5] as

$$BR(K_L \to \pi^0 \nu\bar{\nu}) = 1.94 \times 10^{-10} \eta^2 A^4 \chi^2(x) \tag{1.12}$$

where $x = m_t/m_W$, $\chi \sim x^{1.2}$, and A is a CKM parameter in Wolfenstien parameterization of equation (1.8). The theoretical estimate of this branching ratio is $\cong 3.0 \times 10^{-11}$ based on the current knowledge of CKM parameters [4, 5]. Due to the uncertainties on the CKM parameters, these predictions still contain an error of $\cong 2\times10^{-11}$. The best published limit to data for the $K_L \to \pi^0\nu\bar{\nu}$ decay is 5.9×10^{-7} (90%CL) from E799-I at Fermi National Accelerator Laboratory (FNAL)[6]. The theoretical uncertainty on the relation between $BR(K_L \to \pi^0\nu\bar{\nu})$ and η, that is uncertainty of $A^4\chi^2(x)$ in equation (1.12), has a magnitude of a few percent[4]. Therefore, by measuring the branching ratio of $K_L \to \pi^0\nu\bar{\nu}$, we can directly determine CKM parameter η with a high accuracy.

1.2 $K_L \to \pi^0\nu\bar{\nu}$ experiment

There are several experiments to measure the branching ratio of $K_L \to \pi^0\nu\bar{\nu}$ decay. These experiments collect $K_L \to \pi^0\nu\bar{\nu}$ decays by detecting two photons originating from a π^0 decay. This raises some difficulties for observing $K_L \to \pi^0\nu\bar{\nu}$.

One difficulty is the existence of many difficult backgrounds sources. The decay modes which can be background are $K_L \to \pi^0\pi^0$, $K_L \to \pi^0\pi^0\pi^0$, $K_L \to \gamma\gamma$, $K_L \to \pi^0\gamma\gamma$, $\Lambda \to n\pi^0$, etc.. Of these backgrounds, the dominant and the most severe background is $K_L \to \pi^0\pi^0 \to 4\gamma$(BR=$9.36\times10^{-4}$) where two gammas were missed. There are following two cases for missing two gammas. One is that gamma miss photon detector, either by going between photon detectors or going through a beam hole in a detector. Therefore, it is important to have a hermetic coverage around the decay region and minimize the beam hole size. Another reason is that photon detector misses detection although gamma hits the photon detector. This effect depends on the inefficiency of photon detector, and this inefficiency is a strong function of the energy of the gamma.

1.3 Inefficiency of photon detector

In this section, we will describe the inefficiency of photon detector. There are two major sources of the inefficiency.

One source of the inefficiency is electro–magnetic interaction, which are punch through effect and sampling effect. A punch through effect is a case where a photon passes through the detector without an interaction. If the length of the detector is l, the inefficiency due to the punch through effect is described by:

$$\text{Inefficiency} = e^{-\sigma\cdot\rho\cdot l}, \tag{1.13}$$

where σ is a normalized cross section(cm^2 /g) and ρ is the density(g/cm^3). The cross section depends on the energy of the photon and the $(\sigma\cdot\rho)^{-1}$ becomes $\frac{9}{7}\cdot X_0$ (X_0 is the radiation length) at high energy region.

A sampling effect is a case where the deposit energy is below a threshold. For a sampling calorimeter, such as a lead/scintillator sandwich, this effect is larger than a punch through effect because large fraction of the energy deposited in the lead.

Since the electro–magnetic interaction is understood well, the inefficiency by this cause can be estimated reliably by Monte Carlo simulations.

Other cause of the inefficiency is photo–nuclear interaction. The photo–nuclear interaction is a reaction that an incident photon is absorbed by the nucleus and this nucleus emits protons, neutrons, or photons. If only neutrons are released, the incident photon will not be detected. Since this interaction is not easy to simulate well enough, we must directly measure the inefficiency which is caused by this interaction.

1.4 Motivation and Overview

The inefficiency caused by photo-nuclear interaction was measured by the KEK ES171 experiment for photons with energy below 1GeV. Our purpose is to measure the inefficiency caused by photo-nuclear interaction for photons with energy above 1GeV. This measurement is especially important for $K_L \rightarrow \pi^0\nu\bar{\nu}$ experiments which use high energy kaons ($P_K \geq 10$ GeV/c) to take advantage of low detection inefficiency at high photon energy.

This thesis discribes a new experimental result for measurement of the inefficiency of lead/scintillator sandwich and pure CsI crystal, which are typical detector elements for the $K_L \rightarrow \pi^0\nu\bar{\nu}$ experiments. The next chapter will outline an overview of the experimental method used to measure the ineffciency due to photo–nuclear interaction. The details of detector and run condition will be described in Chapter 3. In Chapter 4, we will describe the calibration of the detectors and the correction for the time walk. In Chapter 5, we will discuss the event selection to suppress backgrounds. In Chapter 6, we will present the estimation of the number of background events. Chapter 7 will present the result and Chapter 8 will present the discussion. At last, in Chapter 9, we will give the conclusion of this study.

Chapter 2

Principle of the experiment

In this chapter, we describe the experimental method to measure the inefficiency due to photo–nuclear interaction. In order to measure the inefficiency, we have to know the number of the photo–nuclear interactions and the number of the incident photons.

The dominant source of inefficinecy caused by photo–nuclear interaction is the interaction which releases its energy by emitting multiple neutrons. Therefore, we will detect these neutrons to tag photo–nuclear interactions by surrounding the detector of interest with 8 liquid scintillators (NE213; 5 inch $\phi\times$ 5 inch long).

The neutron detectors are sensitive not only to neutrons but also to photons emerging from the lead/scintillator or the CsI. We can discriminate neutrons from photons by using the following two differences.

One difference is a time-of-flight. By placing the neutron detectors 20 cm apart from the photon detector, and with 1 ns time resolution, we can identify neutrons below 5 MeV from photons by $> 5.8\sigma$.

Another difference is the shape of the pulse from the liquid scintillator. We can discriminate between neutrons and photons with measuring the shape difference.

We will obtain the number of the incident photons and their energies by using the tagged photons which is decsribed in Section 3.1.

The inefficiency due to photo–nuclear interaction is :

$$\textbf{Inefficiency} = \frac{N_{pn}}{N_\gamma \cdot Accep.}, \tag{2.1}$$

where N_γ is the number of photons entering the detector, N_{pn} is the number of events due to photo–nuclear interaction, and *Accep.* is the acceptance to tag photo–nuclear interactions.

Chapter 3

The Detector and Run

In this Chapter, we describe the photon beam, the detector elements, the trigger and the data acquisition.

3.1 Beam

In order to measure the inefficiency with the sensitivity of $O(10^{-7})$, we had to use a high intensity photon beam. We used the Laser Electron Photon beam line at SPring8.[7]

In the SPring8 BL33LEP beam line, the 350 nm Argon laser beam is injected head-on to the 8 GeV electron beam in the storage ring. Photons from the backward-compton scattering can have its energy up to 2.4 GeV. The recoiled electrons are bent into the inner side of the storage ring by the bending magnet. The momentum of the electron after the scattering is measured by tagging counters which were placed at the inner side of the storage ring (Fig. 3.1). The tagging counters consist of 2 hodscope planes with 10 plastic scintillators each as shown in Fig. 3.1. The energy of photon, E_γ, is calculated as :

$$E_\gamma = 8(\mathrm{GeV}) - E_{tag}, \tag{3.1}$$

where E_{tag} is the energy of the scattered electron measured by the tagging counters. Using the tagging counter, one can measure the energy of photons between 1.5 GeV and 2.4 GeV in about 200 MeV bins.

The rate of the tagged photons was typically 8.0×10^4 Hz for 100 mA of electrons in the storage ring.

3.2 Detector elements and layout

Figure 3.2 shows a schematic drawing of all the elements in our detector and Fig. 3.3 shows an array of the detectors surrounding the photon detector. A summary of the characteristics of our detector is listed in Table 3.1. Each detector elements is described in this section.

3.2.1 Photon detector

Two kinds of photon detectors are used in the experiment.

One is a CsI calorimeter. The CsI calorimeter consists of 9 CsI(pure) crystals. The size of each CsI crystal is 5 cm × 5 cm × 50 cm, which corresponds to 27 X_0 long. The total size of the CsI calorimeter is 15 cm × 15 cm × 50 cm, which corresponds to about 2 R_M (R_M:Moliére radius). Each CsI crystal is viewed by a 1.5 inch Hamamatsu R5330 phototube.

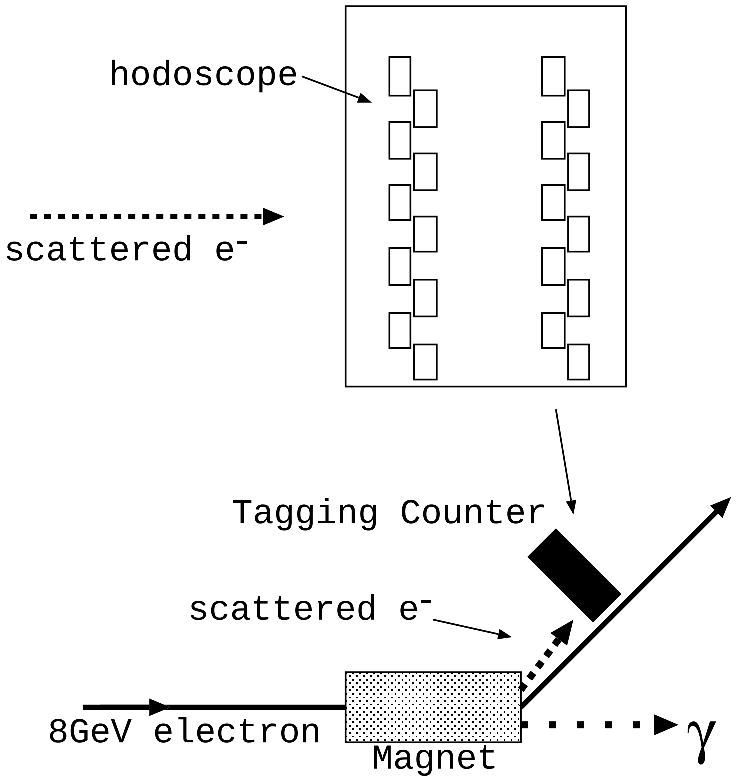

Figure 3.1: A brief sketch of tagging counter.

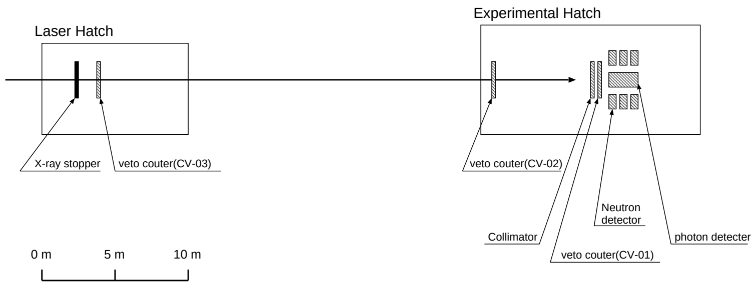

Figure 3.2: A brief sketch of detector location.

Table 3.1: The summary of detector characteristic.

Photon detector	
·CsI :	The size of one CsI(pure) block is 5 cm × 5 cm × 50cm. The total size is 15 cm × 15 cm × 50 cm with 9 CsI crystals which corresponds with $27X_0$ and about $2R_M$.
·lead/scint. :	Each module is a sandwich of 16 sheets of 1 mm lead and 5 mm scintillator. The cross section is 15 cm × 15 cm. The total detector consists of 3 modules which corresponds to $10.2X_0$.
Charge veto	
·CV-01 :	15 cm × 20 cm × 1 cm plastic scintillator.
·CV-02 :	This charge veto counter is used by LEPS group which is made of a plastic scintillator.
·CV-03 :	15 cm × 20 cm × 1 cm plastic scintillator.
·CV-04 :	45 cm × 33 cm × 1 cm plastic scintillator.
·CV-05 :	45 cm × 33 cm × 1 cm plastic scintillator.
·CV-06 :	40 cm × 33 cm × 1 cm plastic scintillator.
·CV-07 :	40 cm × 33 cm × 1 cm plastic scintillator.
Collimator	
This consists of 2 CsI(pure) crystals with a total size of 12 cm × 10 cm × 6 cm. There is a 3cm ϕ hole at the center.	
Neutron detector	
The NE213 liquid scintillator with 5 inch ϕ× 5 inch long (56.5 cm with PMT).	

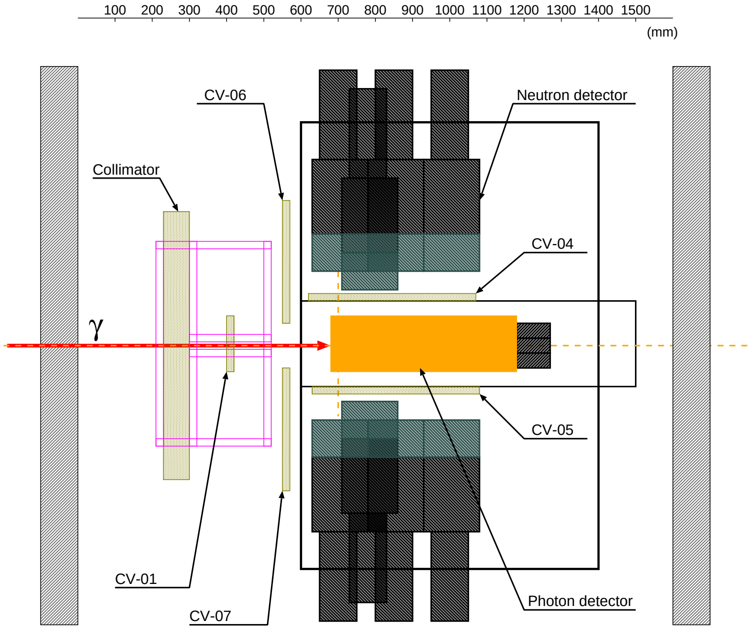

Figure 3.3: A top view of our detectors.

Another is a lead/scintillator sandwich type detector. This detector consists of 3 lead/scintillator modules. One module consists of 16 sheets of 1 mm lead and 5 mm plastic scintillator with 15 cm $\times$ 15 cm. The total detector length is 28.8 cm which corresponds to 10.2 X_0. Each lead/scintillator module is viewd by a 2.4 inch Hamamatsu H1661 phototube through a light guide.

3.2.2 Neutron detector

In oder to measure neutrons which were emitted by the photo–nuclear interaction, we used 8 neutron detectors in the experiment. Each neutron detector consist of 1.6 liters of NE213 liquid scintillator filled in a cylindrical vessel with 5 inch $\phi\times$ 5 inch long (12.7 cm $\phi\times$ 12.7 cm long). Each neutron detector is equipped with a 5 inch Hamamatsu R1250 phototube. These neutron detectors surronded the photon detector as shown in Fig. 3.2 to get a large acceptance for the photo–nuclear interaction. For the lead/scintillator run, 9/7 X_0 (3.6 cm) from the front of the lead/scintillator was aligned to the center of the second neutron detector array from the upstream because the 9/7 X_0 correspond to the averrage length of the photon interaction (Fig. 3.4 right). For the CsI run, we aligned the 9/7 X_0 (2.4 cm) from the front of the CsI detector to the center of the upstream neutron detector, because of a space constraint (Fig. 3.4 left).

3.2.3 Collimater

In order to define the photon beam size, we used an active collimater made of CsI which has a 30 mm diameter hole. The size of the collimater is 12 cm (W) $\times$ 10 cm (H) $\times$ 6 cm (D). This collimator consists of 2 pure CsI crystals which were viewed by 4 phototubes. The collimater was located 338 mm upstream of the edge of front neutron detector.

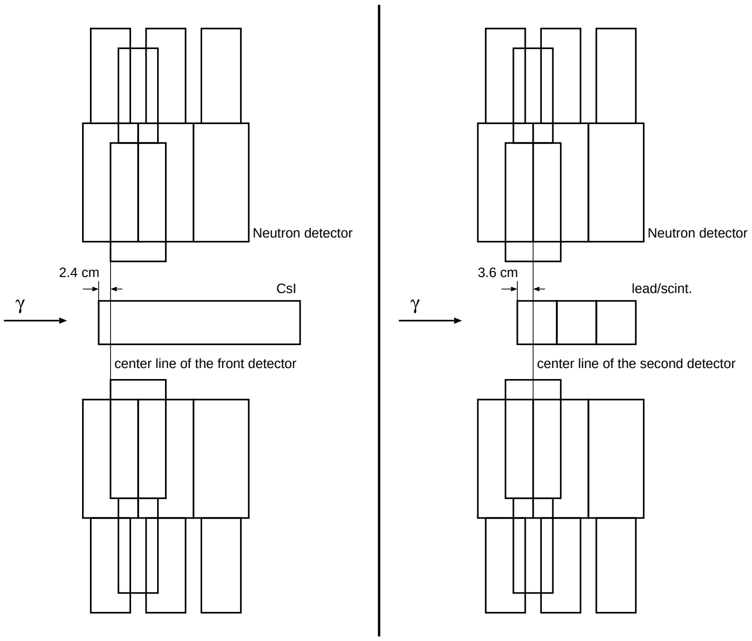

Figure 3.4: The schematic view of the relative location between the photon detctor and the neutron detectors. The CsI detector (left) was located by aligning the 9/7 X_0 (2.4 cm) length from the front face with the center of the front neutron detector. The lead/scintillator (right) was located by aligning the 9/7 X_0 (3.6 cm) length from the front face with the center of the second neutron detector.

3.2.4 Veto counters

There were 7 veto counters in the experiment. Two charge veto counters (CV-01 and CV-02) detected charged particles from interactions of photons with materials placed in the upstream. The CV-03 shown in Fig. 3.2 detects charged particles from interactions of photons in 2mm lead used to absorb X-rays from the storage ring. The CV-04, CV-05, CV-06 and CV-07 detect charged particles which may enter the neutron detectors.

Each charge veto conter is made of plastic scintillator and each size is shown in Table 3.1.

3.3 Trigger

Two kinds of triggers are used for the experiment. One is Tag-sigma trigger. This trigger is used to count the number of incident photons and it is prescaled by a factor 33. The Tag-sigma trigger requires hits in the tagging counters and no hits in CV-03 counter. Another trigger called EG-bar trigger is used to collect candidate events for photo–nuclear interaction. The EG-bar trigger requires hits in the tagging counters, no hits in CV-03, at least one hit in the neutron counter and the energy deposit in the photon detector to be less than a certain threshold.

Tagging counters are required to have at least one hit in the front and at least one hit in the rear.

Figure 3.5 shows the trigger logic.

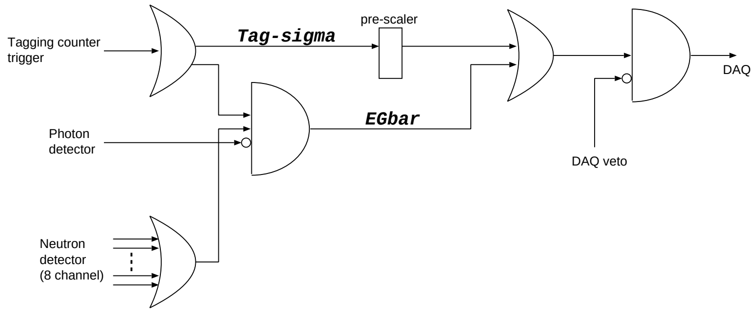

Figure 3.5: A sketch of the trigger logic. Tag-sigma trigger requires hits in the tagging counter, and no hits in the charge veto counter (CV-03).

3.4 Data acquisition

The data acquisition system had following features.

- Read out through a LeCroy FERA DATA bus
- CPU module and Memory module on VME
- Network data transfer

In the experiment, the typical data size was about 60 bytes per event. The read out rate is 1.8 kHz with the dead time of 0.28 ms per event.

3.5 Run

The data was taken from October 13 (2001) to October 16 (2001).

The maximum current of the SPring8 storage ring was 100 mA with 1/12 filling + 10 bunches mode during this period.

For each photon detector, we collected data for about 30 hours.

Chapter 4

Detector calibration and correction

The gain of each channel was calibrated by using cosmic rays or a radiation source. After the calibration, we corrected the TDC data of the neutron detectors because there was a correlation between ADC counts and TDC counts due to a time walk.

The following sections will describe the detail of the detector calibration and the time walk correction.

4.1 Detector calibration

4.1.1 CsI

The calibration was carried out in two stages. First path was to calibrate the relative gain between the 9 crystals using the response for a Minimum Isonizing Particle (MIP) in cosmic rays. Figure 4.1 shows the setup for the calibration run. In this calibration, we used the cosmic rays penetrating a crystal vertically, so that, the energy loss in the CsI is 28 MeV for the 5cm path length. We determined the relative gain by matching the muon peak of the ADC distribution with the energy loss in the CsI.

The second path was to determine the absolute gain. We define the sum of ADC counts of each crystal after the relative gain correction as :

$$E_{sum} = \sum_{i=1}^{9} (\text{relative gain})_i \cdot (ADCcounts)_i. \tag{4.1}$$

Figure 4.2 shows the correlation between E_{sum} and the energy of the incident photon calculated by the tagging counter hit, E_{tag}. The E_{tag} is :

$$E_{tag} = -0.1674 \cdot itag + 3.340\text{GeV}, \tag{4.2}$$

where $itag$ is a number of the row of the tagging counter hodscope (Fig. 5.1). We determined the absolute gain to match $E_{sum} \times$ (absolute gain) with E_{tag}. From the fitting result on Fig. 4.2, we obtained the relation, $E_{tag} = 1.299 \cdot E_{sum}$. In the following, we use $1.299 \cdot E_{sum} (\equiv E_{tot})$ as the total energy deposit in the CsI detector.

4.1.2 Lead/scintillator

First, we calibrated the relative gain between the two lead/scintillator modules using the MIPs where the energy loss in scintillators of one module is 16 MeV.

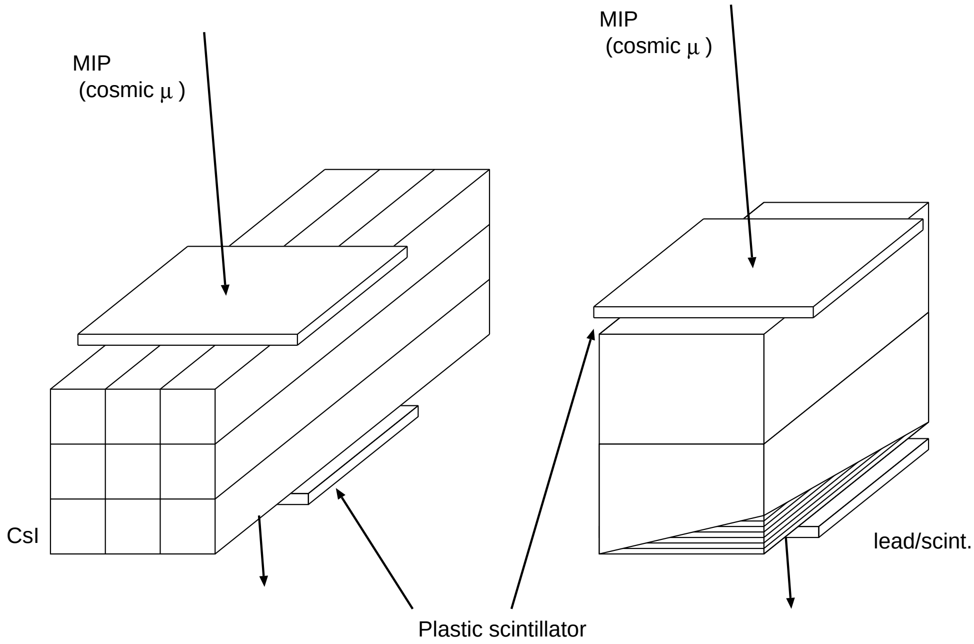

Figure 4.1: A brief sketch of the setup of the calibration run for CsI (left) and lead/scintillator (right). The upper and lower plastic scintillators were used to trigger on penetrating cosmic rays.

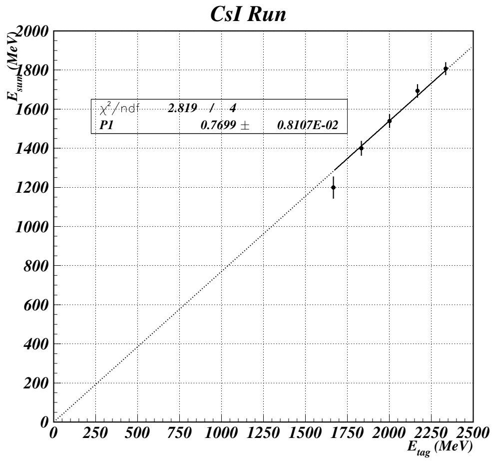

Figure 4.2: The correlation between E_{sum} and E_{tag}. This plot is fitted for $f(x) = P1 \cdot x$. The absolute gain is determined to tune $E_{sum} \times$ (absolute gain) to E_{tag}.

We define E_{sum} as the sum of energy deposit in the two upstream modules ;

$$E_{sum} = \sum_{i=1}^{2} (\text{relative gain})_i \cdot (ADCcounts)_i. \tag{4.3}$$

Since the total radiation lengths of the two modules is 6.1 X_0, there is a leakage of the electro-magnetic shower. Taking the leakage into account, we estimated the energy deposit in the two modules with EGS monte calro simulation. Figure 4.3 shows the correlation between the energy deposit in the scintillators of the two modules, E_{sc}, and the incident energy of gamma, E_γ. In the high energy region, E_{sc}/E_γ is smaller because of a larger energy leakage. We fitted it for a function $E_{sc} = P1 \cdot E_\gamma - P2 \cdot E_\gamma^{P3}$, and obtained the result, $E_{sc} = 0.3241 \cdot E_\gamma - 0.00423 \cdot E_\gamma^{1.463}$. Figure 4.4 shows the correlation between E_{sum} and E_{sc} using $E_\gamma = E_{sc}$. By fitting, we obtained $E_{sum} = 0.7149 \cdot E_{sc}$. The relation between E_{sc} and the total energy deposit in the two modules including the lead, E_{dep}, is [8]:

$$E_{sc} = 0.3381 \cdot E_{dep} - 0.1491\,\text{MeV}. \tag{4.4}$$

Therefore, the total energy deposit in the lead/scintillator E_{tot} is :

$$E_{tot} \equiv E_{dep} = \frac{E_{sum}/0.715 + 0.1491}{0.3381}.\,\text{MeV} \tag{4.5}$$

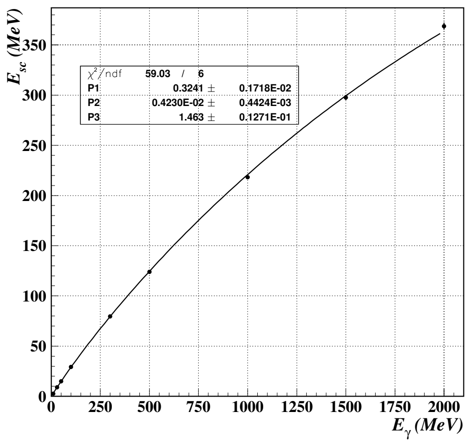

Figure 4.3: The correlation between E_{sc} and the incident photon energy E_γ calculated by EGS monte calro simulation.

4.1.3 Neutron detector

The neutron detectors were calibrated by using a ^{60}Co source. Figure 4.5 shows the setup for the calibration of neutron detectors.

Figure 4.7 (left) shows the distribution of the energy depoisted in the neutron detector calculated by the EGS simulation. However, the distribution of the deposited energy measured in the calibration run is smeared due to the energy resolution, as shown in Fig. 4.7 (right). Therefore we fitted it for the function :

$$F(x) = \sum_i P3 \cdot N_i \cdot e^{-\frac{1}{2}\left(\frac{P1 \cdot x - E_i}{\sigma_i}\right)^2}, \tag{4.6}$$

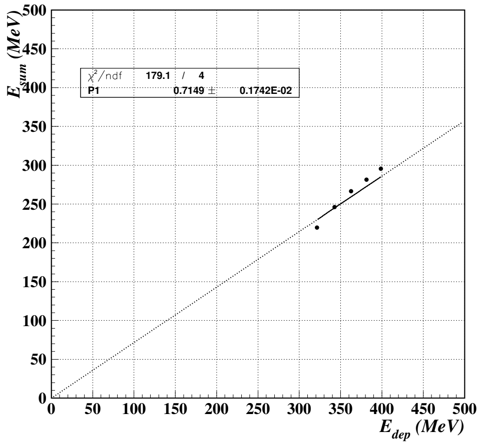

Figure 4.4: The correlation between E_{sum} and E_{tag} for the lead/scintillator run. This plot is fitted with $f(x) = P1 \cdot x$.

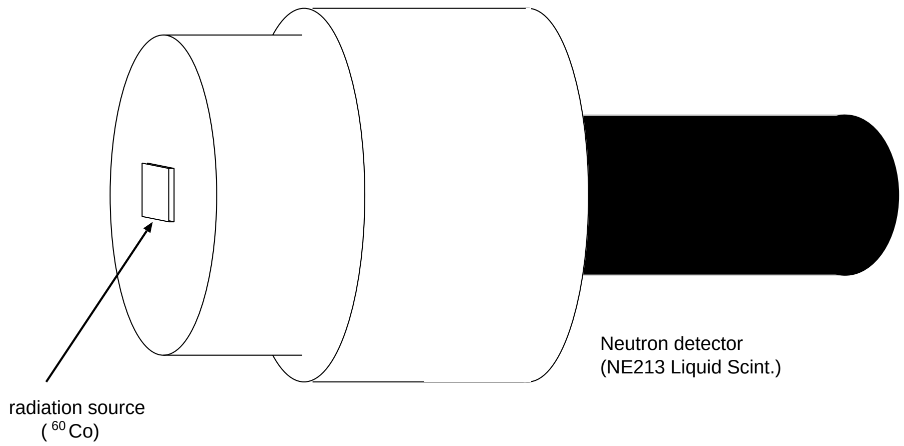

Figure 4.5: The setup of the calibration of neutron detectors. The ^{60}Co radiation source was placed at the center of the front face of the detector.

where N_i is the number of events in the E_i's bin obtained by the EGS simulation, and $\sigma_i = P2 \cdot \sqrt{E_i}$. In this function, the free parameter, $P1$, means the gain for the neutron detector.

We calibrated each neutron detector for 3 different high voltages with this method and determined a proper HV for a desired gain by using an extraplotion.

The energy scale from this calibration can be applied to photons but not to neutrons, because the response of the liquid scintillator is not linear for $E_{neutron} < 5$ MeV. In this thesis, we will use the energy scale for photons.

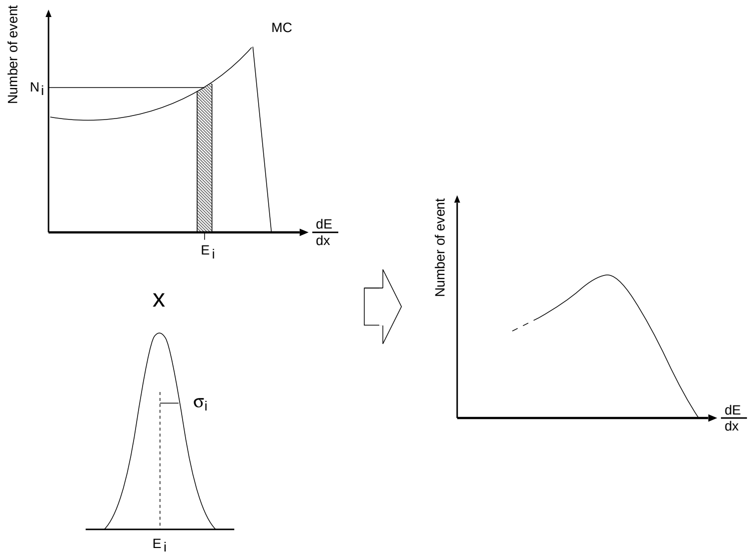

Figure 4.6: The real distribution of the deposited energy was calculated by the EGS monte calro simulation. In order to obtain a gain of a neutron detector, we fit the distribution of ADC counts for the real distribution smeared with $P2 \cdot \sqrt{E_i}$ resolution.

4.2 Time walk correction

Since there is a correlation between ADC counts and TDC counts due to a time walk, we corrected the TDC counts of the neutron detectors.

The plot on the left column in Figure 4.8 shows the correlation between ADC counts and TDC counts of the neutron detector for Tag-sigma trigger events. Most of the particles hitting the neutron detector in the Tag-sigma trigger events are photons. We fitted this correlation for the expression:

$$\mathbf{TDC_{fit}} = C_1 \cdot (\mathbf{ADC})^{-1/2} - C_2 \cdot \mathbf{ADC} + C_3, \tag{4.7}$$

where C_1,C_2 and C_3 are free parameters which have positive values. We determined the value of C_1,C_2 and C_3 by fitting the data, then we defined the TDC value after correction:

$$\mathbf{TDC_{corr}} = \mathbf{TDC_{raw}} - \mathbf{TDC_{fit}}. \tag{4.8}$$

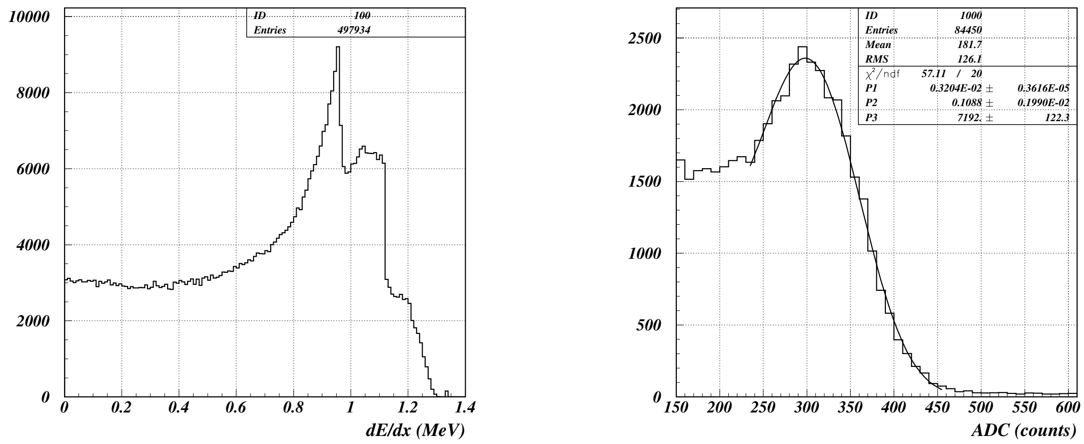

Figure 4.7: The left plot shows the distribution of the deposited energy in the neutron detector which is calculated by the EGS Monte Calro simulation. The photon energies from ^{60}Co are 1.173 MeV and 1.333 MeV. The right plot shows the ADC distribution of the neutron detector. We fitted this distribution by the function (4.6).

The plot on the right colunm in Figure 4.8 shows the distribution between ADC counts and TDC counts after the correction. The value of $\mathrm{TDC_{corr}}$ is tuned to be zero for photons.

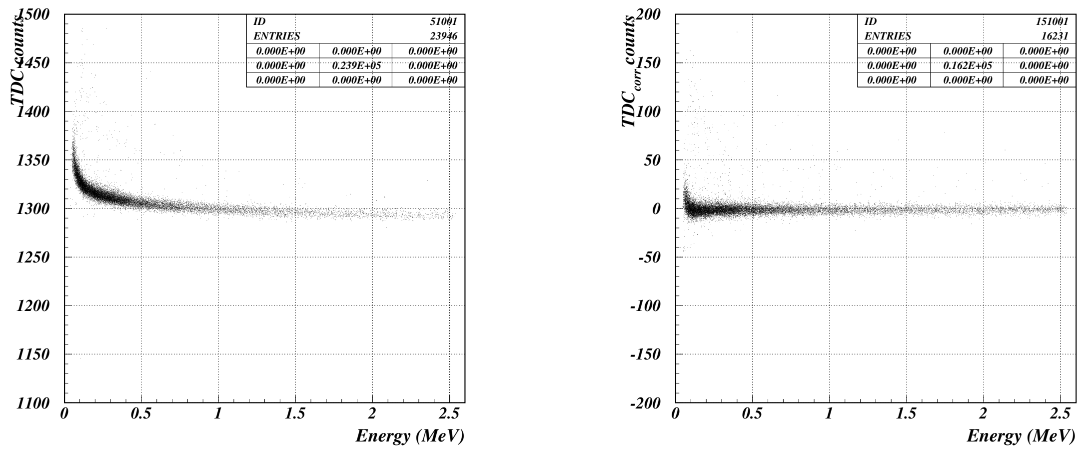

Figure 4.8: The left plot shows the correlation between the ADC counts and TDC counts of the neutron detector. The right plot shows the correlation between the ADC counts and TDC counts after the correction described in the text. In the energy region above 0.15 MeV, the time walk effect is corrected well but, in the energy region below 0.15 MeV, the time walk effect still remains.

Chapter 5

Event selection

In order to identify the photo–nuclear interactions, we require the following conditions.

- EGbar trigger event
- At least two neutron detectors has a hit
- No hits in veto counters
- The total energy deposited in the photon detector is less than a certain threshold

In this Chapter, we will discuss these event selections. In section 5.4, we will describe the acceptance for the photo–nuclear interaction. The normalization of the inefficiency will be described in the section 5.5.

5.1 Tag-sigma, EGbar

First, we required that there is only one hit in each tagging counter hodoscope, and that those two hits are in the same row. We numbered the row of the hodscope as *itag*, as shown in Figure 5.1.

We decided whether each event is the Tag-sigma event or the EGbar event by using the TDC for the EGbar signal. Figure 5.2 shows the TDC distribution of the EGbar. The EGbar events have a peak at ~ 650 counts because the TDC start signal was made by EGbar signal itself. Therefore we defined the events in the peak around 500 counts $<$ TDC $<$ 750 counts as the EGbar trigger events and the event in the other region as the Tag-sigma trigger events.

5.2 Neutron selection

We discriminated neutrons from photons by using the time-of-flight and the difference of the shape of the emmited pulse from the liquid scintillator.

The neutron detection relies mainly on detecting the recoiled proton in (n,p) scattering processes. Because the scattered protons deposit a large energy in a localized area of the scintillator, they saturate the excited status of the scintillator. This creates a slow component in the light emission. On the other hand, photons will give normal light emission which is dominated by a fast component. In order to extract the slow component, we split the scintillator output, and delayed one of them to measure the pulse charge with two different ADC gate timings. As shown in Fig. 5.3, this is equivalent to measuring the pulse charge with two different gate widths. For photons, the ADC counts with “wide” gate and “narrow” gate are the same. However, for neutrons, the ADC counts with “narrow” gate is smaller

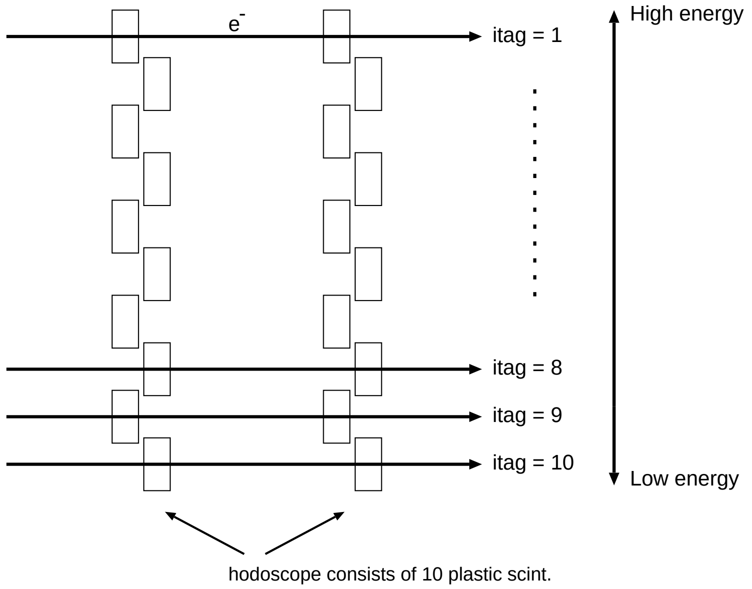

Figure 5.1: The brief skech of the taggig counter cut. We require the coincidence of the same row hit in the two hodoscopes and the single multiplicity of the *itag*.

than the ADC counts with "wide" gate, because the full pulse is not being covered. Here, we defined the n/w value :

$$\mathrm{n/w} = \frac{\text{“narrow” ADC counts}}{\text{“wide” ADC counts}}. \tag{5.1}$$

We identified neutrons with the n/w cut and the time of flight (TOF) cut as described below.

5.2.1 n/w cut

Since there is also a correlation between the n/w value and the ADC counts, we corrected the n/w value. Figure 5.4 (left) shows the correlation between the ADC counts and the n/w values for the Tag-sigma events. We fitted this correlation for the function[10]:

$$\mathrm{n/w_{fit}} = Q_1 \cdot (\mathrm{ADC})^{-1} + Q_2 + Q_3 \cdot (\mathrm{ADC})^{-1/2} - Q_4 \cdot (\mathrm{ADC}) + Q_5 \cdot (\mathrm{ADC})^{1/2}, \tag{5.2}$$

where Q_1,Q_2,Q_3,Q_4 and Q_5 are free positive parameters. We defined the corrected n/w value:

$$\mathrm{n/w_{corr}} = \mathrm{n/w_{raw}} - \mathrm{n/w_{fit}}. \tag{5.3}$$

In the following analysis, we will use the n/$\mathrm{w_{corr}}$. Figure 5.4 (right) shows the distribution after the correction.

Figure 5.5 (left) shows the distribution of the n/$\mathrm{w_{corr}}$. The events near zero are photons and the events in the peak around 0.1 are neutrons. We fitted this distribution for the sum of two Gaussians. In order to reduce the contamination from photons and to obtain high acceptance for neutrons, we required n/$\mathrm{w_{corr}}$ to satisfy :

$$(\mu_{\mathrm{neutron}} - 3\sigma_{\mathrm{neutron}}) < \mathrm{n/w_{corr}} < (\mu_{\mathrm{photon}} - 3\sigma_{\mathrm{photon}}), \tag{5.4}$$

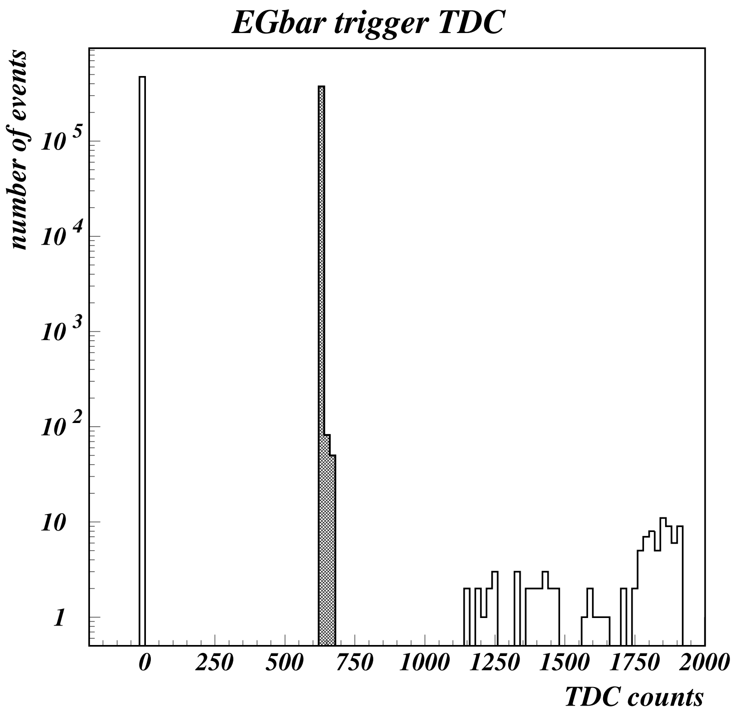

Figure 5.2: The TDC distribution of the EGbar trigger signal. The events in the dark region are defined as the EGbar trigger events in the offline analysis. The events in other region are defined as the Tag-sigma trigger events.

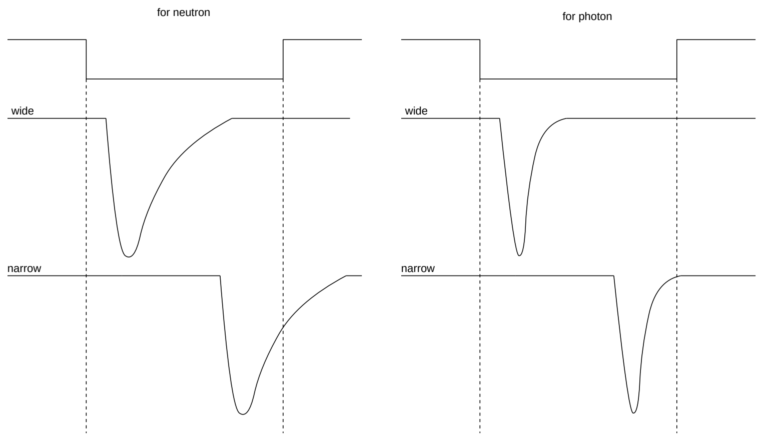

Figure 5.3: A brief sketch of the method to discriminate between neutrons and photons detected by the neutron detectors. The "wide" value is measured with a normal timing and the narrow value is measured by delaying the input signal. The left figure shows a pulse for a neutron and the right figure shows a pulse for a photon. Because the pulse for a neutron has a slow component, the "wide" value is samller than the "narrow" value. For photons, the "wide" value is same as the "narrow" value.

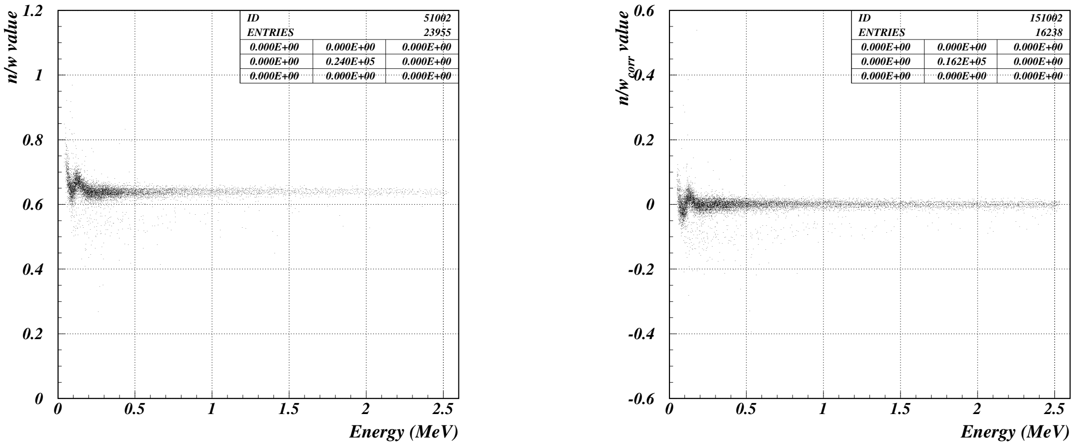

Figure 5.4: The left plot shows the correlation between the ADC counts and the n/w values. The right plot shows the correlation between the ADC counts and the n/w values after the correction described in the text. However, there is a distribution like snake in the energy region < 0.15 MeV.

where μ_{neutron} and μ_{photon} are the mean values of the fitted Gaussians for neutrons and photons, respectively, and σ_{neutron} and σ_{photon} are the standard deviations for neutrons and photons, respectively.

Since n/w$_{\text{corr}}$ for the neutron events has an energy dependence and there is a snake distribution in the energy region $E_{n-det.} < 0.15$ MeV, we decided the upper cut on n/w$_{\text{corr}}$ separately for three energy regions, 0.15 MeV $\leq E_{n-det.} <$ 0.5 MeV, 0.5 MeV $\leq E_{n-det.} <$ 1.0 MeV and 1.0 MeV $\leq E_{n-det.}$. It will be discussed in section 8.1 whether the selection $E_{n-det.} > 0.15$ MeV is proper. Figure 5.5 (left) also shows the accepted region by this cut. Figure 5.5 (right) shows the energy dependence of the n/w value with the neutron region by this cut. We will estimate the number of the background events due to mis-identification by this n/w cut in Section 6.1.

The n/w cut for each neutron detector is summarized in Table 5.1 and Table 5.2.

5.2.2 TOF cut

A cut on time of flight (TOF) was applied on the TDC$_{\text{corr}}$ value. As described in Section 4.2, the TDC$_{\text{corr}}$ value is tuned to be zero for photons. Figure 5.6 (left) shows the distribution of the TDC$_{\text{corr}}$ value. We also fitted this distribution for a sum of two Gaussians. We define the TOF cut as :

$$(\mu_{\text{photon}} + 3\sigma_{\text{photon}}) < \text{TDC}_{\text{corr}} < (\mu_{\text{neutron}} + 3\sigma_{\text{neutron}}), \tag{5.5}$$

where μ_{neutron} and μ_{photon} are the mean values of the fitted Gaussians for neutrons and photons, respectively, and σ_{neutron} and σ_{photon} are the standard deviations for neutrons and photons, respectively.

The TDC$_{\text{corr}}$ value for the neutron events also has an energy dependence, so we decide three different lower cuts on the TDC counts for energy regions, $0.15 \leq E_{n-det.} <$ 0.5 MeV, $0.5 \leq E_{n-det.} <$ 1.0 MeV and $1.0 \leq E_{n-det.}$ MeV. The upper cut is kept the same for all energy regions.

Figure 5.6 (right) shows the energy dependence of the TDC counts and the neutron region selected by this cut. The TOF cut for each neutron detector is summarized in Table 5.3 and Table 5.4.

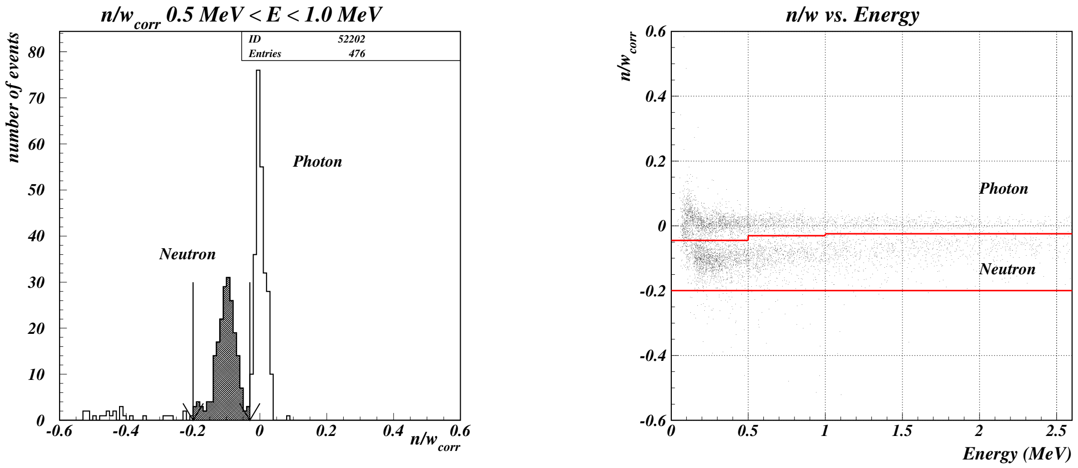

Figure 5.5: The plot of the n/w value for the energy region $0.5 \leq E_{n-det.} < 1.0$ MeV (left). The neutron region is defined by $(\mu_{\text{neutron}} - 3\sigma_{\text{neutron}}) < \text{n/w}_{\text{corr}} < (\mu_{\text{photon}} - 3\sigma_{\text{photon}})$. The right plot shows the energy dependence of the n/w cut. The upper boundary vairies with the energy region.

Table 5.1: The summary of the n/w cut for each neutron detector on the CsI runs.

Energy region	Neutron detector 1	Neutron detector 2
$0.15 \leq E_{n-det.} < 0.5$ MeV	$-0.1763 < \text{n/w}_{\text{corr}} < -0.03455$	$-0.1999 < \text{n/w}_{\text{corr}} < -0.04475$
$0.5 \leq E_{n-det.} < 1.0$ MeV	$-0.1763 < \text{n/w}_{\text{corr}} < -0.02318$	$-0.1999 < \text{n/w}_{\text{corr}} < -0.03047$
$1.0 \leq E_{n-det.}$ MeV	$-0.1763 < \text{n/w}_{\text{corr}} < -0.01998$	$-0.1999 < \text{n/w}_{\text{corr}} < -0.02479$
Energy region	Neutron detector 3	Neutron detector 4
$0.15 \leq E_{n-det.} < 0.5$ MeV	$-0.1903 < \text{n/w}_{\text{corr}} < -0.03825$	$-0.1732 < \text{n/w}_{\text{corr}} < -0.04419$
$0.5 \leq E_{n-det.} < 1.0$ MeV	$-0.1903 < \text{n/w}_{\text{corr}} < -0.02567$	$-0.1732 < \text{n/w}_{\text{corr}} < -0.03024$
$1.0 \leq E_{n-det.}$ MeV	$-0.1903 < \text{n/w}_{\text{corr}} < -0.01876$	$-0.1732 < \text{n/w}_{\text{corr}} < -0.02055$
Energy region	Neutron detector 5	Neutron detector 6
$0.15 \leq E_{n-det.} < 0.5$ MeV	$-0.1741 < \text{n/w}_{\text{corr}} < -0.03584$	$-0.1758 < \text{n/w}_{\text{corr}} < -0.04001$
$0.5 \leq E_{n-det.} < 1.0$ MeV	$-0.1741 < \text{n/w}_{\text{corr}} < -0.02647$	$-0.1758 < \text{n/w}_{\text{corr}} < -0.02676$
$1.0 \leq E_{n-det.}$ MeV	$-0.1741 < \text{n/w}_{\text{corr}} < -0.02111$	$-0.1758 < \text{n/w}_{\text{corr}} < -0.02253$
Energy region	Neutron detector 7	Neutron detector 8
$0.15 \leq E_{n-det.} < 0.5$ MeV	$-0.1684 < \text{n/w}_{\text{corr}} < -0.03697$	$-0.2223 < \text{n/w}_{\text{corr}} < -0.05450$
$0.5 \leq E_{n-det.} < 1.0$ MeV	$-0.1684 < \text{n/w}_{\text{corr}} < -0.02799$	$-0.2223 < \text{n/w}_{\text{corr}} < -0.03287$
$1.0 \leq E_{n-det.}$ MeV	$-0.1684 < \text{n/w}_{\text{corr}} < -0.01711$	$-0.2223 < \text{n/w}_{\text{corr}} < -0.02543$

Table 5.2: The summary of the n/w cut for each neutron detector on the lead/sicntillator runs.

Energy region	Neutron detector 1	Neutron detector 2
$0.15 \leq E_{n-det.} < 0.5$ MeV	$-0.1707 <$ n/w$_{\rm corr} < -0.03643$	$-0.1910 <$ n/w$_{\rm corr} < -0.04667$
$0.5 \leq E_{n-det.} < 1.0$ MeV	$-0.1707 <$ n/w$_{\rm corr} < -0.02453$	$-0.1910 <$ n/w$_{\rm corr} < -0.03050$
$1.0 \leq E_{n-det.}$ MeV	$-0.1707 <$ n/w$_{\rm corr} < -0.02196$	$-0.1910 <$ n/w$_{\rm corr} < -0.02400$
Energy region	Neutron detector 3	Neutron detector 4
$0.15 \leq E_{n-det.} < 0.5$ MeV	$-0.1879 <$ n/w$_{\rm corr} < -0.03814$	$-0.2026 <$ n/w$_{\rm corr} < -0.04556$
$0.5 \leq E_{n-det.} < 1.0$ MeV	$-0.1879 <$ n/w$_{\rm corr} < -0.02508$	$-0.2026 <$ n/w$_{\rm corr} < -0.03096$
$1.0 \leq E_{n-det.}$ MeV	$-0.1879 <$ n/w$_{\rm corr} < -0.01683$	$-0.2026 <$ n/w$_{\rm corr} < -0.02009$
Energy region	Neutron detector 5	Neutron detector 6
$0.15 \leq E_{n-det.} < 0.5$ MeV	$-0.1656 <$ n/w$_{\rm corr} < -0.03774$	$-0.1666 <$ n/w$_{\rm corr} < -0.04346$
$0.5 \leq E_{n-det.} < 1.0$ MeV	$-0.1656 <$ n/w$_{\rm corr} < -0.02845$	$-0.1666 <$ n/w$_{\rm corr} < -0.02814$
$1.0 \leq E_{n-det.}$ MeV	$-0.1656 <$ n/w$_{\rm corr} < -0.01833$	$-0.1666 <$ n/w$_{\rm corr} < -0.02242$
Energy region	Neutron detector 7	Neutron detector 8
$0.15 \leq E_{n-det.} < 0.5$ MeV	$-0.1561 <$ n/w$_{\rm corr} < -0.03174$	$-0.1987 <$ n/w$_{\rm corr} < -0.05888$
$0.5 \leq E_{n-det.} < 1.0$ MeV	$-0.1561 <$ n/w$_{\rm corr} < -0.02380$	$-0.1987 <$ n/w$_{\rm corr} < -0.03403$
$1.0 \leq E_{n-det.}$ MeV	$-0.1561 <$ n/w$_{\rm corr} < -0.01813$	$-0.1987 <$ n/w$_{\rm corr} < -0.02434$

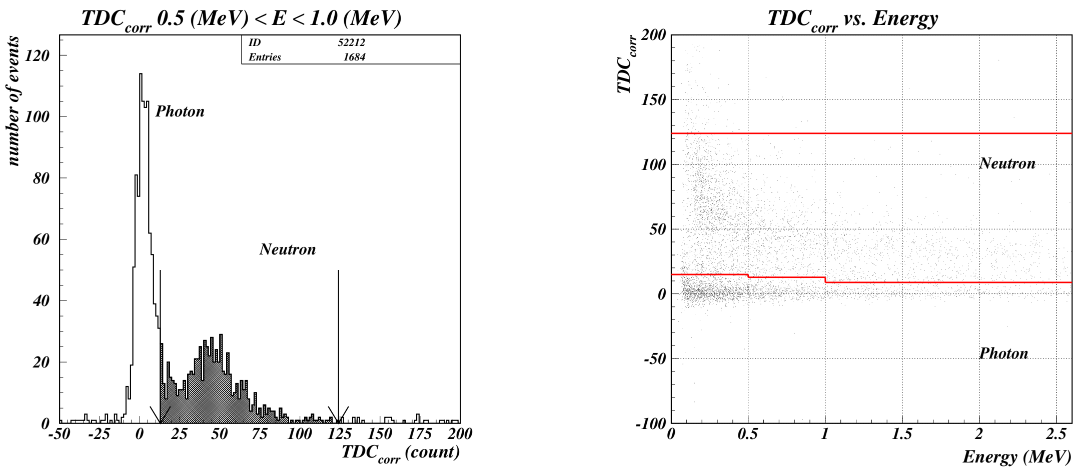

Figure 5.6: The plot of the TDC counts for the energy region $0.5 \leq E_{n-det.} < 1.0$ MeV (left). The neutron region is defined by $(\mu_{\rm photon} + 3\sigma_{\rm photon}) <$ TDCcorr $< (\mu_{\rm neutron} + 3\sigma_{\rm neutron})$. The plot on the right shows the energy dependence of the TOF cut. The lower boundary is different between the energy regions.

Table 5.3: The summary of the TOF cut for each neutron detector on the CsI runs.

Energy region	Neutron detector 1	Neutron detector 2
$0.15 \leq E_{n-det.} < 0.5$ MeV	$12.99 < \mathrm{TDC_{corr}} < 126.4$	$14.90 < \mathrm{TDC_{corr}} < 124.0$
$0.5 \leq E_{n-det.} < 1.0$ MeV	$11.46 < \mathrm{TDC_{corr}} < 126.4$	$12.87 < \mathrm{TDC_{corr}} < 124.0$
$1.0 \leq E_{n-det.}$ MeV	$8.487 < \mathrm{TDC_{corr}} < 126.4$	$8.824 < \mathrm{TDC_{corr}} < 124.0$
Energy region	Neutron detector 3	Neutron detector 4
$0.15 \leq E_{n-det.} < 0.5$ MeV	$16.03 < \mathrm{TDC_{corr}} < 192.1$	$17.31 < \mathrm{TDC_{corr}} < 195.5$
$0.5 \leq E_{n-det.} < 1.0$ MeV	$12.30 < \mathrm{TDC_{corr}} < 192.1$	$14.34 < \mathrm{TDC_{corr}} < 195.5$
$1.0 \leq E_{n-det.}$ MeV	$9.879 < \mathrm{TDC_{corr}} < 192.1$	$11.84 < \mathrm{TDC_{corr}} < 195.5$
Energy region	Neutron detector 5	Neutron detector 6
$0.15 \leq E_{n-det.} < 0.5$ MeV	$13.24 < \mathrm{TDC_{corr}} < 142.2$	$12.97 < \mathrm{TDC_{corr}} < 136.6$
$0.5 \leq E_{n-det.} < 1.0$ MeV	$11.14 < \mathrm{TDC_{corr}} < 142.2$	$9.862 < \mathrm{TDC_{corr}} < 136.6$
$1.0 \leq E_{n-det.}$ MeV	$9.662 < \mathrm{TDC_{corr}} < 142.2$	$9.160 < \mathrm{TDC_{corr}} < 136.6$
Energy region	Neutron detector 7	Neutron detector 8
$0.15 \leq E_{n-det.} < 0.5$ MeV	$13.76 < \mathrm{TDC_{corr}} < 118.4$	$16.12 < \mathrm{TDC_{corr}} < 105.9$
$0.5 \leq E_{n-det.} < 1.0$ MeV	$10.07 < \mathrm{TDC_{corr}} < 118.4$	$12.74 < \mathrm{TDC_{corr}} < 105.9$
$1.0 \leq E_{n-det.}$ MeV	$8.200 < \mathrm{TDC_{corr}} < 118.4$	$10.89 < \mathrm{TDC_{corr}} < 105.9$

Table 5.4: The summary of the TOF cut for each neutron detector on the lead/sicntillator runs.

Energy region	Neutron detector 1	Neutron detector 2
$0.15 \leq E_{n-det.} < 0.5$ MeV	$16.24 < \text{TDC}_{\text{corr}} < 152.7$	$20.19 < \text{TDC}_{\text{corr}} < 158.9$
$0.5 \leq E_{n-det.} < 1.0$ MeV	$10.25 < \text{TDC}_{\text{corr}} < 152.7$	$16.20 < \text{TDC}_{\text{corr}} < 158.9$
$1.0 \leq E_{n-det.}$ MeV	$6.293 < \text{TDC}_{\text{corr}} < 152.7$	$8.309 < \text{TDC}_{\text{corr}} < 158.9$
Energy region	Neutron detector 3	Neutron detector 4
$0.15 \leq E_{n-det.} < 0.5$ MeV	$21.20 < \text{TDC}_{\text{corr}} < 160.3$	$23.03 < \text{TDC}_{\text{corr}} < 144.1$
$0.5 \leq E_{n-det.} < 1.0$ MeV	$17.79 < \text{TDC}_{\text{corr}} < 160.3$	$20.80 < \text{TDC}_{\text{corr}} < 144.1$
$1.0 \leq E_{n-det.}$ MeV	$12.64 < \text{TDC}_{\text{corr}} < 160.3$	$15.10 < \text{TDC}_{\text{corr}} < 144.1$
Energy region	Neutron detector 5	Neutron detector 6
$0.15 \leq E_{n-det.} < 0.5$ MeV	$20.13 < \text{TDC}_{\text{corr}} < 130.1$	$20.12 < \text{TDC}_{\text{corr}} < 132.8$
$0.5 \leq E_{n-det.} < 1.0$ MeV	$16.96 < \text{TDC}_{\text{corr}} < 130.1$	$12.55 < \text{TDC}_{\text{corr}} < 132.8$
$1.0 \leq E_{n-det.}$ MeV	$12.56 < \text{TDC}_{\text{corr}} < 130.1$	$9.330 < \text{TDC}_{\text{corr}} < 132.8$
Energy region	Neutron detector 7	Neutron detector 8
$0.15 \leq E_{n-det.} < 0.5$ MeV	$19.72 < \text{TDC}_{\text{corr}} < 123.4$	$23.25 < \text{TDC}_{\text{corr}} < 121.3$
$0.5 \leq E_{n-det.} < 1.0$ MeV	$11.09 < \text{TDC}_{\text{corr}} < 123.4$	$16.53 < \text{TDC}_{\text{corr}} < 121.3$
$1.0 \leq E_{n-det.}$ MeV	$7.638 < \text{TDC}_{\text{corr}} < 123.4$	$12.56 < \text{TDC}_{\text{corr}} < 121.3$

5.3 Veto cut

5.3.1 Charge veto cut

We have to remove the events where the tagged photons interacted at the upstream and did not enter the photon detector. We rejected these events by detecting charged particles from the interaction. We also have to discriminate neutral particles from charged particles entering the neutron detector. The seven charge veto counters are located as shown in Fig. 3.2 and Fig. 3.3.

In the analysis, we cut on the ADC and the TDC of all the charge veto counters. We required the ADC counts to be less than 3σ(pedestal) where σ(pedestal) is obtained by fitting the pedestal peak for a Gaussian. The TDCs were required to have no hits in an 800 ns time window.

The pedestals were taken for CsI runs and lead/scintillator runs, separately.

5.3.2 Collimator cut

We applied similar cuts on the collimator by using its ADC and TDC.

After the collimator cut and the charge veto cut, 67.3 % of the events survived for the CsI runs and 65.7 % of the events survived for the lead/scintillator runs.

5.3.3 Other veto cut

For the lead/scintillator runs, we require additional cut on the energy deposit in the third lead/scintillator module. We defined the total energy deposit in the lead/scintilator as the sum of the energy deposit in the first and the second module. Therefore when we require the total energy deposit in the photon detector to be less than a threshold, there still may be some events which deposited more energy in the third modules.

In order to remove such events, we require the ADC counts of the third lead/scintillator module to be less than 3σ(pedestal). The σ(pedestal) is also obtained with fitting the pedestal peak for a Gaussian.

5.4 Acceptance

The acceptance for the photo–nuclear interaction was estimated from the distribution of the multiplicity of the neutron detector hits. We assumed that the distribution of the multiplicity follows a poisson distribution. Since we require the condition, "At least two neutron detecters has a hit", the acceptance of the photo–nuclear interaction is calculated by :

$$Acceptance = 1 - (1 + \mu) \cdot e^{-\mu}, \tag{5.6}$$

where μ is a mean value of the poisson distribution.

In order to obtain the multiplicity mean, we considered the multiplicity with some different conditions although there are little events with the signal selection. We used six different conditions for the total energy deposit in the photon detector, 250MeV $< E_{tot} <$ 300MeV, 200MeV $< E_{tot} <$ 250MeV, 150MeV $< E_{tot} <$ 200MeV, 100MeV $< E_{tot} <$ 150MeV, 50MeV $< E_{tot} <$ 100MeV, and $E_{tot} <$ 50MeV. We estimated the mean value fitting the multiplicity in the region, multiplicity ≥ 2, for a poisson distribution when the degree of the freedom is ≥ 1. When the degree of the freedom is zero, we calculated the mean value as following:

$$\mu = 3 \times \frac{P(3, \mu)}{P(2, \mu)} = 3 \times \frac{N_3}{N_2}, \tag{5.7}$$

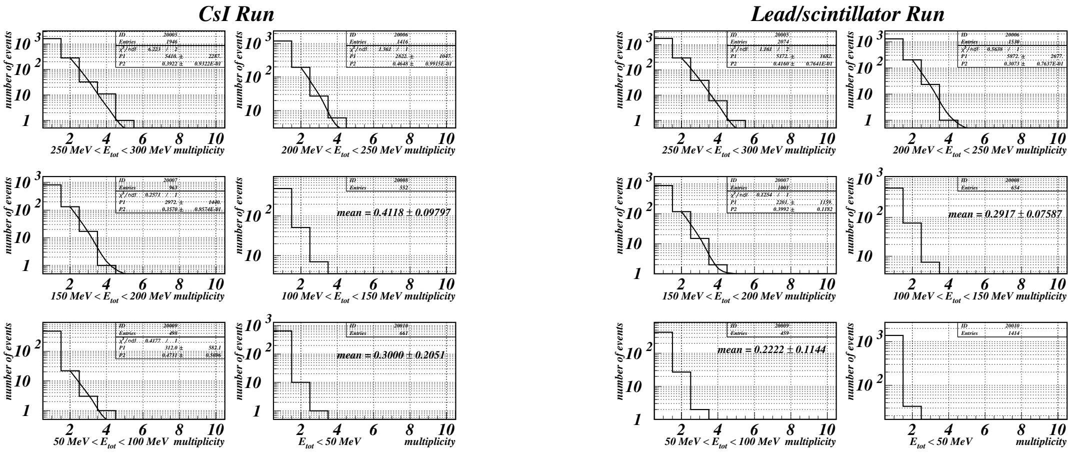

Figure 5.7: These plots show the distributions of the multiplicity of the neutron detector which has a neutron hit for the CsI runs (left) and the lead/scintillator (right). We fitted each for a poisson distribution but we calculated the mean value as following the equation (5.7) if there is no number of dimensions of the freedom.

where $P(n, \mu)$ is a poisson distribution with the mean value μ. Figure 5.7 shows the distributions of the multiplicity for each E_{etot} cut for the CsI detector (left) and the lead/scintillator (right).

The mean value of the multiplicity is shown as a function of the E_{tot} cut for the CsI detector (Fig. 5.8 left) and the lead/scintillator (Fig. 5.8 right). The μ and the acceptaince for the photo–nuclear interaction are summarized in Table 5.5.

Table 5.5: The summary of the acceptance of the photo–nuclear interaction.

	CsI Runs	lead/scintillator Runs
μ	0.4102 ± 0.0358	0.3881 ± 0.0329
Acceptance	$(6.43 \pm 0.97)\%$	$(5.84 \pm 0.87)\%$

5.5 Normalization

In order to select clean events with incident photons hitting the photon detector, we require the following condition for the normalization.

- Hit in the tagging counter
- Tag-sigma trigger event
- Charge veto cut and collimator cut

The first 2 cuts are exactly the same as for Tag-sigma events. The destribution of the total energy deposit after required these conditions are shown in Figure 5.9 (left) for the CsI run and Fig, 5.9 (right) for the lead/scintillator run.

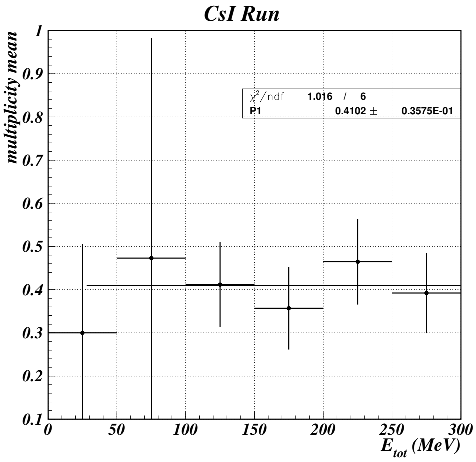

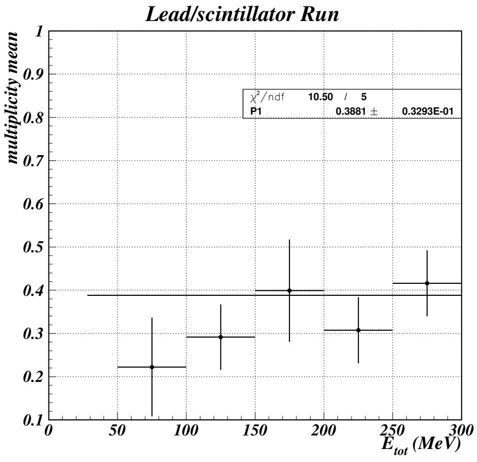

Figure 5.8: The left plot shows the correlation between the mean of the multiplicity and E_{tot} for the CsI detector. The mean value is independent from the threshold value, so we fitted it for a constant. The average value of the mean is 0.4102 ± 0.0358. The right plot shows the correlation between the mean of the multiplicity and E_{tot} for the lead/scintillator. The average value of the mean is 0.3881 ± 0.0329.

We required additional cut to reject "false tag events" where the photons did not enter the photon detector. We required $Etot > 500$ MeV for the CsI run and $Etot > 200$ MeV for the lead/scintillator run. The number of photons in the accepted region is 1.77×10^7 events for the CsI run and 1.56×10^7 events for the lead/scintillator run. Correcting for a prescale factor 33 for the Tag-sigma trigger, we obtained the number of incident photons for each photon detector as shown in Table 5.6.

Table 5.6: The summary of the number of incident photons.

CsI Runs	lead/scintillator Runs
5.83×10^8 events	5.15×10^8 events

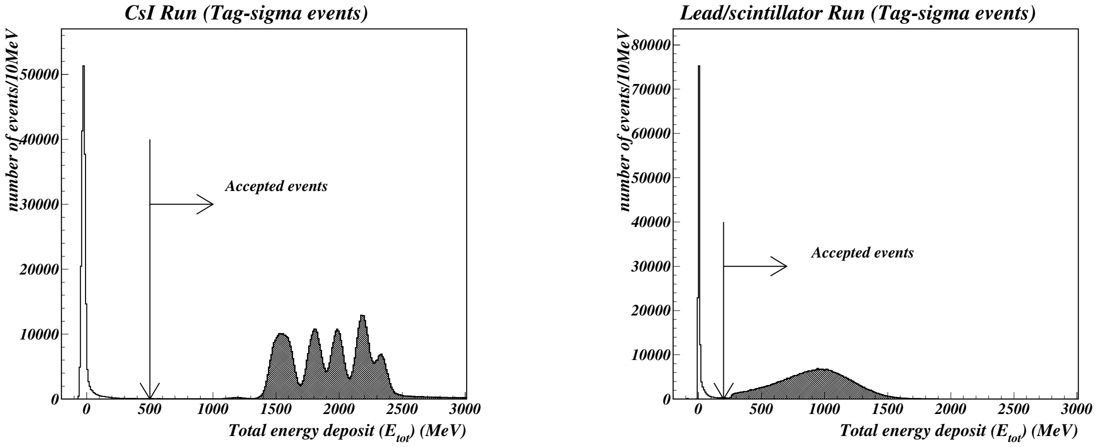

Figure 5.9: These plots show the distribution of the total energy deposit in the CsI (left) and the lead/scintillator (right) with some requirements for the normalization described in the text. The events in the dark region were accepted. Since the energy resolution of the CsI crystals is better than the resolution of the tagging counter (it is about 50 MeV), we can find the peak when we required a hit in the tagging counter. On the other hand, we can not find its peak for the lead/scintillator run because of shower leakage.

Chapter 6

Background estimation

In this chapter, we will estimate the number of background events. In this analysis, as described in the previous chapter, we made the following requirements to select the signal;

- EGbar trigger event,
- at least two neutron detectors has a hit,
- no hits in veto counters, and
- the total energy deposited in the photon detector is less than a certain threshold

There are two major background types which can satisfy the above requirements.

1. There are one or two neutron mis-identification. (**Mis-ID**)
2. There are false hits in the tagging counters, or a photon interacted in the upsteam. Therefore, a photon does not come down the beam line. In addition, there are two accidental hits in the neutron detector. (**False tag + 2 accidental neutrons**)

The following sections will describe the estimation of the number of these background events.

6.1 Mis-ID

If photons enter the neutron detector and satisfy the neutron selection cuts, these events will become background events. Figure 6.1 shows a scatter plot between n/w$_{\mathrm{corr}}$ values and TDC counts. In order to estimate the number of these background events, we analyzed the n/w$_{\mathrm{corr}}$ distribution in the Band A (Fig. 6.1) where we required the same signal selection cuts except for the cuts on the number of neutrons and n/w$_{\mathrm{corr}}$ cut. Figure 6.2 shows a sample plot of the n/w$_{\mathrm{corr}}$ distribution for a CsI run. We estimated the number of these background events using two different methods.

In one method, we required additional condition that at least one neutron detector has a hit. We then looked at n/w$_{\mathrm{corr}}$ − TOF distribution for other neutron detector. We assumed the events lying in the box on the other side of the photon peak are photons. The number of events in the box was 1 for the CsI runs and 0 for the lead/scintillator runs. Assuming that the photon peak is symmetric in n/w$_{\mathrm{corr}}$, we estimated the number of these events as the number of background events in the neutron region.

In another method, we used the number of neutrons in the signal region, N_{ij}^{sig}, in the energy region cut j ($j = 1$ means $0.15 < E_{n-det.} < 0.5$ MeV, $j = 2$ means $0.5 < E_{n-det.} < 1.0$ MeV and $j = 3$ means

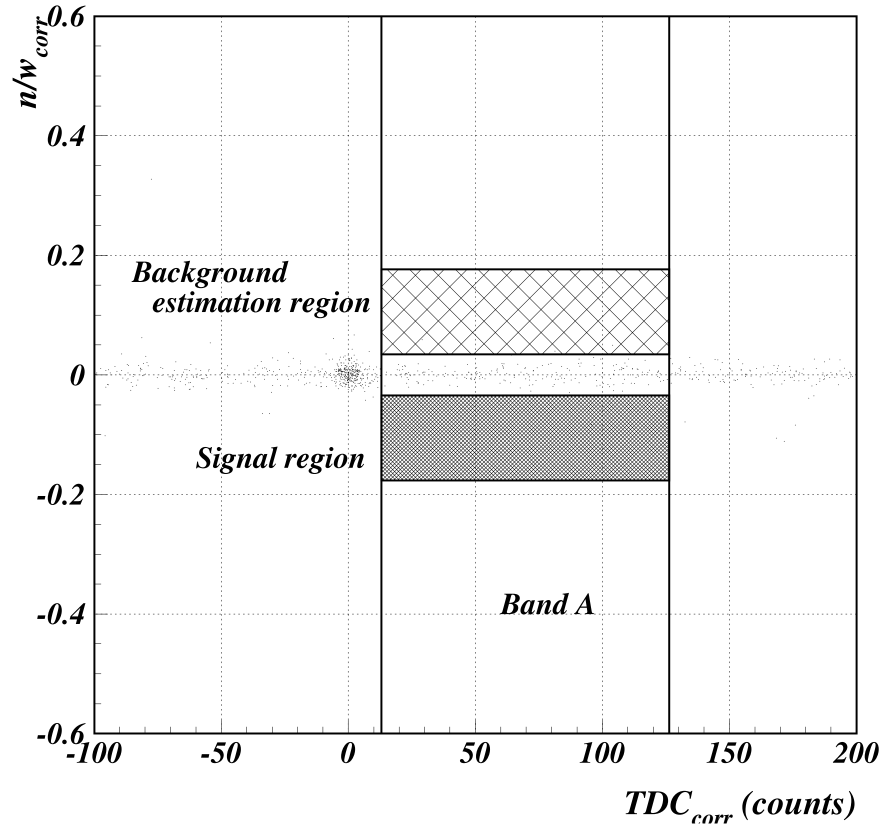

Figure 6.1: A scatter plot between n/w_{corr} and TDC counts with signal cut which does not include the condition of the number of neutron hit (CsI run). We estimated the number of background using the events in the opposite box to the photon peak.

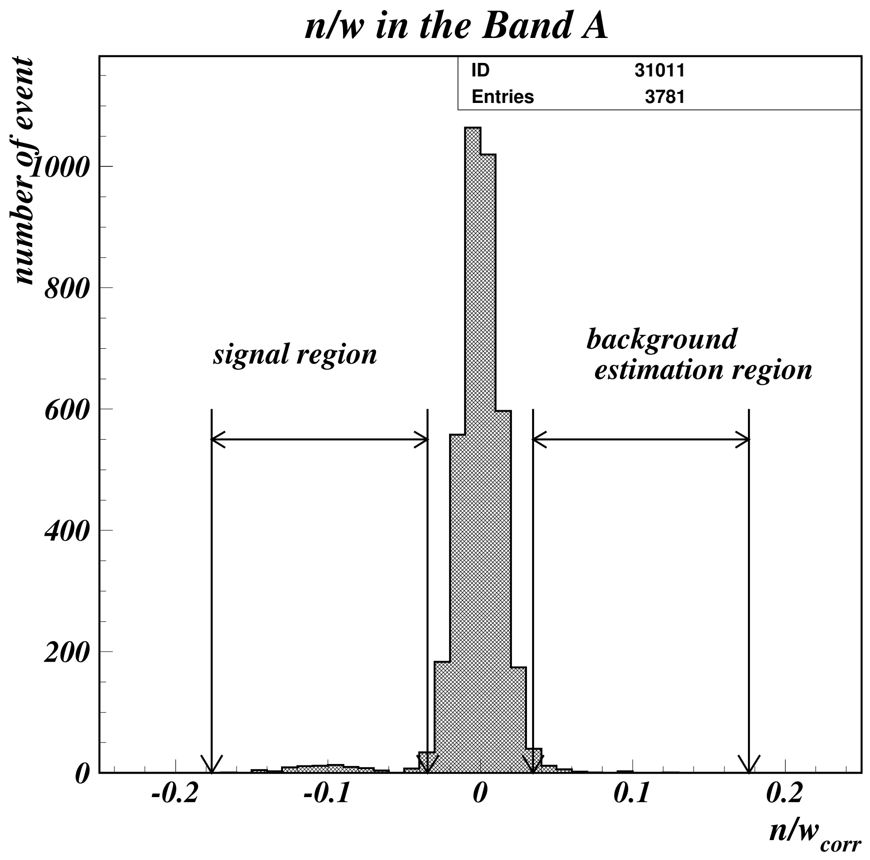

Figure 6.2: A distribution of the n/w_{corr} in the Band A with signal cut which does not include the cut of the number of neutron hit (CsI run).

$1.0 \leq E_{n-det.}$ MeV) for the neutron detector i ($i = 1, .., 8$) and the number of photons in the signal region, N_{ij}^{bgs}. We counted N_{ij}^{sig} and N_{ij}^{bgs} using the events in the Band A. In order to obtain N_{ij}^{bgs}, we fitted the photon peak for a Gaussian and calculated the number of events which are smeared into the signal region as :

$$N_{ij}^{bgs} = \int_{(sig.region)_{ij}} \text{Gaussian}_{ij} \; d(\text{n/w}_{\text{corr}}). \tag{6.1}$$

Figure 6.3 shows the distribution of the n/w_{corr} in the Band A with the fitting result. We defined $N_{ij}^{sig'} = N_{ij}^{sig} - N_{ij}^{bgs}$. After the calculation of $N_{ij}^{sig'}$ and N_{ij}^{bgs}, we summed up it and obtained $N_{i}^{sig'}$ and N_{i}^{bgs} :

$$N_{i}^{sig} = \sum_{j=1}^{3} N_{ij}^{sig'}, \tag{6.2}$$

$$N_{i}^{bgs} = \sum_{j=1}^{3} N_{ij}^{bgs}. \tag{6.3}$$

The number of events N_{i}^{sig} and N_{i}^{bgs} is summarized in Table 6.1.

For one EGbar event which satisfies the charge veto cut, the collimator cut and the cut on total energy deposit in the photon detector, the average number of photons misidentified as neutrons is :

$$W_i = \frac{N_i^{bgs}}{M}, \tag{6.4}$$

where M is the number of EGbar events with the above condition. Similarly, the average number of neutrons is :

$$R_i = \frac{N_i^{sig}}{M}. \tag{6.5}$$

The number of background events caused by misidentifying one photon as a neutron is :

$$N_{either} = M \times \left(\sum_{i} \sum_{j(j \neq i)} W_i \cdot R_j \right), \tag{6.6}$$

where the sum is carried out for 8×7 combinations. The number of background events caused by miisidentifying two photons as neutorons is :

$$N_{both} = M \times \left(\sum_{i} \sum_{j(j \neq i)} W_i \cdot W_j \right), \tag{6.7}$$

where the sum is carried out for ${}_8C_2$ combinations. The total number of background events are $N_{either} + N_{bath}$.

We obtained $M = 1.2 \times 10^6$ events for the CsI runs and $M = 2.7 \times 10^6$ events for the lead/scintillator runs. Therefore, we obtained (0.111 ± 0.027) events for the CsI runs and (0.012 ± 0.005) events for the lead/scintillator runs.

Table 6.1: The number of events N_i^{sig} and N_i^{bgs} estimated by the method in the text.

CsI Run

N_1^{sig}	$=$	115.22 ± 10.74	N_1^{bgs}	$=$	17.78 ± 4.22
N_2^{sig}	$=$	152.05 ± 12.33	N_2^{bgs}	$=$	24.95 ± 5.00
N_3^{sig}	$=$	46.64 ± 6.83	N_3^{bgs}	$=$	23.36 ± 4.83
N_4^{sig}	$=$	68.33 ± 8.27	N_4^{bgs}	$=$	19.67 ± 4.43
N_5^{sig}	$=$	69.62 ± 8.34	N_5^{bgs}	$=$	35.48 ± 5.96
N_6^{sig}	$=$	86.12 ± 9.28	N_6^{bgs}	$=$	16.88 ± 4.11
N_7^{sig}	$=$	94.84 ± 9.74	N_7^{bgs}	$=$	26.16 ± 5.11
N_8^{sig}	$=$	99.47 ± 9.97	N_8^{bgs}	$=$	15.53 ± 3.94

Lead/scintillator Run

N_1^{sig}	$=$	109.79 ± 10.48	N_1^{bgs}	$=$	1.21 ± 1.10
N_2^{sig}	$=$	93.93 ± 9.69	N_2^{bgs}	$=$	1.07 ± 1.04
N_3^{sig}	$=$	282.46 ± 16.81	N_3^{bgs}	$=$	8.54 ± 2.92
N_4^{sig}	$=$	237.39 ± 15.41	N_4^{bgs}	$=$	11.61 ± 3.41
N_5^{sig}	$=$	96.86 ± 9.84	N_5^{bgs}	$=$	0.14 ± 0.37
N_6^{sig}	$=$	159.58 ± 12.63	N_6^{bgs}	$=$	1.42 ± 1.19
N_7^{sig}	$=$	157.83 ± 12.56	N_7^{bgs}	$=$	1.17 ± 1.08
N_8^{sig}	$=$	93.31 ± 9.66	N_8^{bgs}	$=$	5.69 ± 2.38

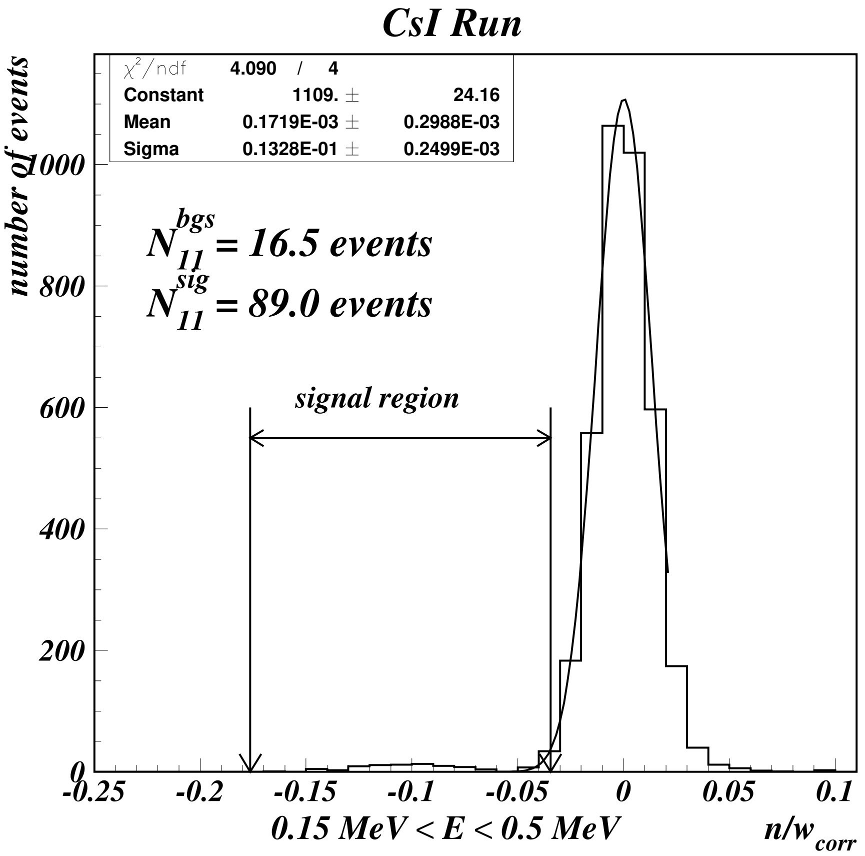

Figure 6.3: This plot shows a distribution of the events in the Band A with same signal selection without the number of neutron cut (CsI run). We estimated the number of the photons in the neutron region from the shape of the tail by fitting the peak for a Gaussian. For the neutron detector 1 on the CsI runs, we obtained 16.5 events as N_1^{bgs} calculated by the method described in the text.

6.2 False tag + 2 accidental neutron

6.2.1 False tag

There are two major types of the false tag. One type is the event where the electron hitting the tagging counter came from the non-straight sections of the storage ring. One such example is a bremsstrahlung due to residual gas in the storage ring. In such a case, the photons do not come down the beam line. Another type is the event that the backward-Compton scattering photon interacted with a material and got lost.

The latter events can be vetoed with the charge veto counters. However, there still are the former events. After applying the charge veto cut, we estimate the number of false tag events by using EGbar trigger events. Assuming the events in the pedestal peak as the false tag events (Fig. 6.4), about 8 % of the EGbar events are false tag events. The contribution of photo–nuclear interaction in this pedestal peak is negligible, as described later. We will also discuss this estimation in section 8.2.

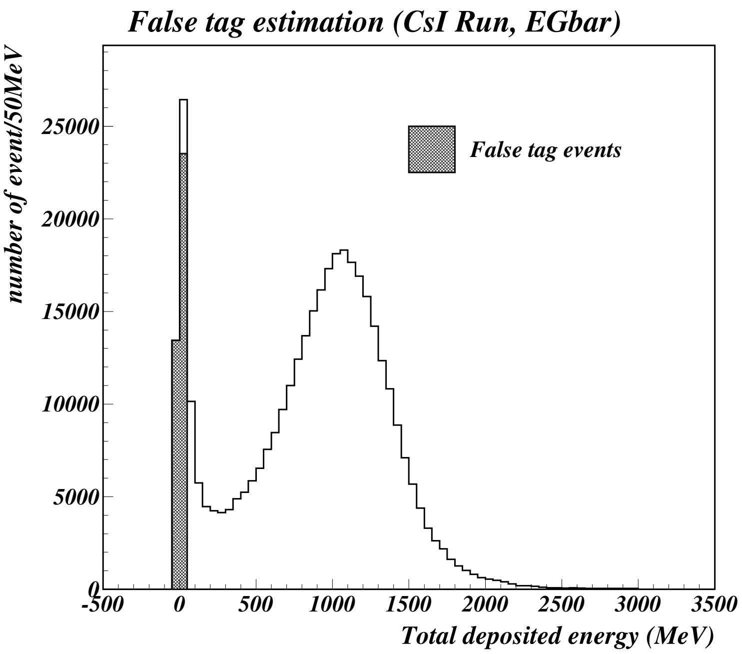

Figure 6.4: This plot shows the distribution ot the total deposited energy in the CsI detector. The events in the dark region are the false tag events.

6.2.2 accidental neutron

We estimate the rate of accidental neutrons by using the TDC distribution for the neutron detector. Figure 6.5 shows the TDC distribution of the events with the EGbar cut, the charge veto cut, the collimator cut and the n/w$_{\rm corr}$ cut. We assume the events in the TDC window, 200 ch < TDC$_{\rm corr}$ < 400 ch (corresponding to 40 ns time window), as accidental neutrons. We obtained the number of accidental neutron events for each 8 neutron detector and found m'_{bgs} = 16 events. The total rate of an accidental neutron, f, is described by :

$$f = \frac{m'_{bgs}}{N \times 40\mathrm{ns}}, \tag{6.8}$$

where N is the number of the EGbar events which satisfy the charge veto and the collimator cut, and it is 1.2×10^5.

Since the typical range of the TOF cut of the neutron selection is 30 ns, the number of events which have two accidental neutrons, m_{bgs}, is:

$$m_{bgs} = N \times (f \times 30\mathrm{ns})^2 = (1.2 \pm 0.3) \times 10^{-3}\mathrm{events}. \tag{6.9}$$

The number of the background events is :

$$(\text{false tag rate}) \times m_{bgs} = (9.6 \pm 2.4) \times 10^{-5},$$

and thus negligible.

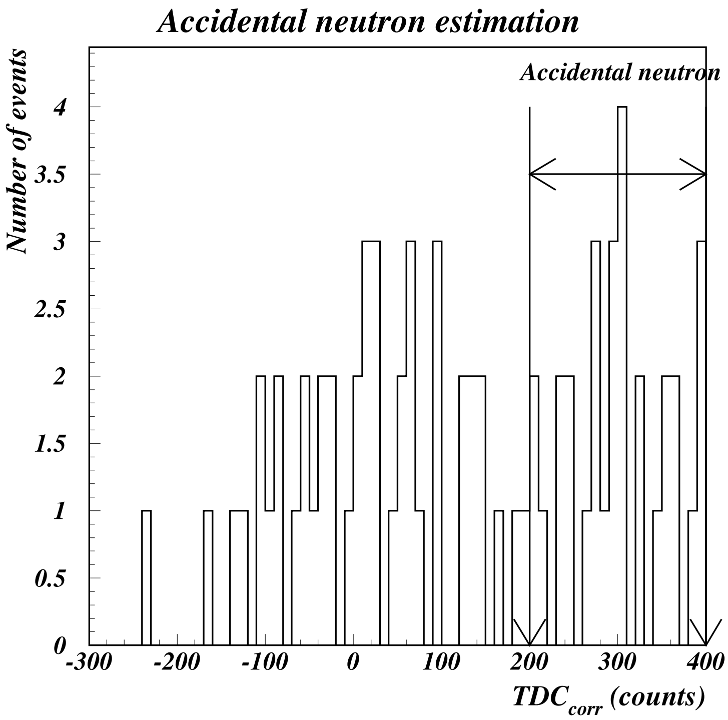

Figure 6.5: This plot shows the distribution of the TDC after the signal selection without the number of neutron cut. We estimate the number of the accidental neutrons by using the events in the TDC window 200 ch < $\mathrm{TDC_{corr}}$ < 400 ch.

Chapter 7

Result

In this chapter, we describe the result of the measurement of the photon detection inefficiency due to photo–nuclear interaction at $1.5 < E_\gamma < 2.4$ GeV. We set the threshold equivalent to 10 MeV incident photon energy.

7.1 CsI Run

We obtained 12 candidate events for the photo–nuclear interaction with an expected background of 1 event. We subtract this background and get the inefficiency,

$$\text{Inefficiency} = \frac{11}{5.83 \times 10^8 \times 0.0643} = (2.93 \pm 0.89_{(stat.)}{}^{+1.15}_{-0.44}{}_{(sys.)}) \times 10^{-7} \tag{7.1}$$

We estimated three major sources of the systematic error.

The largest error is from the estimation of the mean of the multiplicity (μ). We re-estimated the μ with a different method. Figure 7.1 shows the correlation between the mean of the multiplicity and E_{tot} for the CsI detector. We fitted it for $f(x) = P1 + P2 \cdot x$ instead of a constant, and obtained $\mu = 0.3349$ at $E_{tot} < 10$ MeV. This lowered the acceptance to 0.048, and changed the result by $+1.06 \times 10^{-7}$.

Other two sources are $\sigma_{\text{acp.}}$ and from the normalization. The error on the acceptance shown in Table 5.5 corresponds to an error of $\pm 0.043 \times 10^{-7}$ on the inefficiency. We also estimated the systematic error from the normalization. We changed the E_{tot} cut which is described in section 5.5 from 100 MeV to 1000 MeV and obtained a relative error $\sigma_{N_\gamma}/N_\gamma = 0.862\%$. This changed the result by $\pm 0.025 \times 10^{-7}$.

The systematic errors are summarized in Table 7.1.

Table 7.1: The systematic error for the CsI runs.

source	$\times 10^{-7}$
$\sigma_{\text{acp.}}$	± 0.443
μ estimation	$+1.06$
Normalization	± 0.025
Total	$^{+1.15}_{-0.44}$

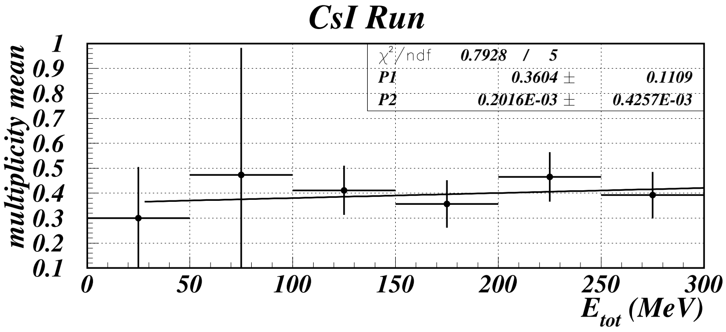

Figure 7.1: This plot shows the correlation between the mean of the multiplicity and E_{tot} for the CsI detector. We fitted it for $f(x) = P1 + P2 \cdot x$ instead of a constant.

7.2 Lead/scintillator Run

In the lead/scintillator runs, there are 25 candidate events for the photo–nuclear interaction with no expected background events. In this experiment, we used the 1mm lead/5mm scintillator module with the total length of 6.1 X_0. The inefficiency is,

$$\text{Inefficiency} = \frac{25}{5.15 \times 10^8 \times 0.0584} = (8.3 \pm 1.7_{(stat.)}{}^{+13.5}_{-1.2}{}_{(sys.)}) \times 10^{-7} \tag{7.2}$$

We also estimated three major sources of the systematic error.

The largest error is from the estimation of the mean of the multiplicity (μ). We re-estimated the μ with the same method as for the CsI runs. Figure 7.2 shows the correlation between the mean of the multiplicity and E_{tot} for the lead/scintillator detector. We fitted it for $f(x) = P1 + P2 \cdot x$ instead of a constant, and obtained $\mu = 0.0314$ at $E_{tot} < 10$ MeV. This lowered the acceptance to 0.00048, and changed the result by $+13.5 \times 10^{-7}$.

Other two sources were estimated by same method as for the CsI runs. The error of the acceptance corresponds to an error of $\pm 1.23 \times 10^{-7}$ on the inefficiency. We changed the E_{tot} cut which is described in section 5.5 from 100 MeV to 250 MeV and obtained the relative error $\sigma_{N_\gamma}/N_\gamma = 0.768\%$. This changed the result by $\pm 0.064 \times 10^{-7}$.

The systematic errors are summarized in Table 7.2.

Table 7.2: The systematic error for the lead/scintillator runs.

source	$\times 10^{-7}$
σacp.	± 1.23
μ estimation	$+13.4$
Normalization	± 0.064
Total	$^{+13.5}_{-1.2}$

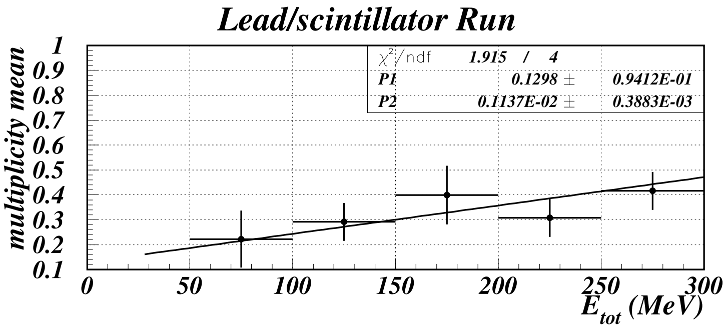

Figure 7.2: This plot shows the correlation between the mean of the multiplicity and E_{tot} for the lead/scintillator detector. We fitted it for $f(x) = P1 + P2 \cdot x$ instead of a constant.

Chapter 8

Discussion

In this chapter, we discuss the result of the inefficiency due to the photo–nuclear interaction.

8.1 $E_{n-det.} \geq 0.15$ MeV cut

We required the condition, $E_{n-det.} \geq 0.15$ MeV, for the signal selection. If most of the signal events are in the $E_{n-det.} < 0.15$ MeV region, the measured inefficiency will be smaller than actual one. We considered whether this selection is proper or not.

We collected the signal events without the cut on $E_{n-det.}$. The distribution of the energy deposit in the neutron detectors of the signal events are shown in Fig. 8.1 (left) for the CsI runs and Fig. 8.1 (right) for the lead/scintillator runs. The threshold of the discriminater for the neutron detector is 0.05 MeV which is a half of the first bin. Since the first bin is the tail of the distribution, the number of events below the discriminater threshold must be less than contents of the first bin. Therefore, the $E_{n-det.} \geq 0.15$ MeV cut was low enough to absorbed neutrons.

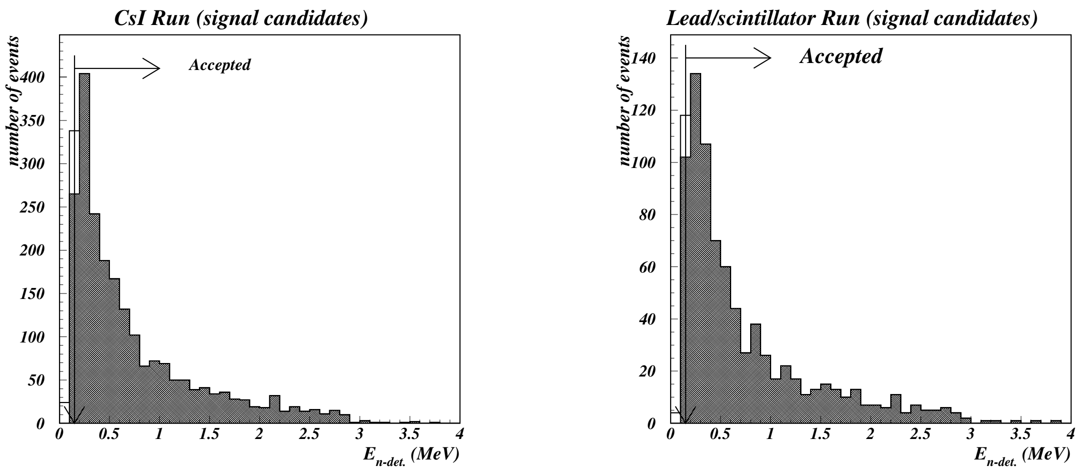

Figure 8.1: These plots show the distribution of the energy deposit in the neutron detectors of the signal events for the CsI run (left) and the lead/scintillator runs (right). We obtained the efficiency 95.8% for the CsI runs and 97.6% for the lead/scintillator runs for $E_{n-det.} \geq 0.15$ MeV cut.

8.2 Estimation of false tag events

In the section 6.2.1, we estimated the number of false tag events as the events in the pedestal peak of the EGbar events (Fig. 6.4).

From the result, we can obtain the number of signal events in the EGbar events. Because EGbar trigger required at least one hit in the neutron detectors, the number of signal events is :

$$N_{signal}(nhit \geq 1) = N_\gamma \cdot (Ineff.) \cdot (1 - e^{-\mu}), \tag{8.1}$$

where N_γ is the number of incident photons, $Ineff.$ is the inefficiency measured in this experiment and μ is the mean of the multiplicity.

For the CsI runs, we calculated $N_{signal}(nhit \geq 1)$ with $N_\gamma = 5.83 \times 10^8$, $Ineff. = 2.97 \times 10^{-7}$ and $\mu = 0.41$ and then obtained $N_{signal}(nhit \geq 1) = 5.82 \times 10^2$. The number of EGbar events is 1.17×10^6 events so that the number of expected false tag events is $1.17 \times 10^6 \times 8\% = 9.4 \times 10^4$ events. Therefore, 0.6 % of the expected false tag events are signal events, and thus is negligible.

For the lead/scintillator runs, we calculated $N_{signal}(nhit \geq 1)$ with $N_\gamma = 5.15 \times 10^8$, $Ineff. = 8.31 \times 10^{-7}$ and $\mu = 0.39$ and then obtained $N_{signal}(nhit \geq 1) = 1.38 \times 10^3$. The number of EGbar events is 2.68×10^6 events so that the number of expected false tag events is $2.68 \times 10^6 \times 8\% = 2.1 \times 10^5$ events. Therefore, 0.7 % of the expected false tag events are signal events, and thus is also negligible.

8.3 Inefficiency vs. E_γ

As shown in section 1.3, the inefficiency is sensitive to the incident photon energy. This time, we measured the inefficiency for the incident photon energy at $1.5 < E_\gamma < 2.4$ GeV. The inefficiency at $E_\gamma < 1$ GeV was measured by the ES171 experiment.[10, 11, 12]

Figure 8.2 shows the inefficiency due to photo–nuclear interaction measured by ES171 and this experiment for the CsI detector. The inefficiency measured by this experiment is on the line extrapolated from the inefficiency at lower energy region.

Figure 8.3 shows the inefficiency due to photo–nuclear interaction measured by ES171 and this experiment for the lead/scintilator detector. The inefficiency measured by this experiment is comparable to the inefficiency at energy region ~ 900 MeV.

8.4 Inefficiency due to electro-magnetic interaction

As described in section 1.3, there is an inefficiency due to electro-magnetic interaction. The inefficiency due to electro-magnetic interaction are a punch through effect and a sampling effect. The punch through effect can be estimated by the cross section of the material of the photon detector. We can also estimate the sampling effect using EGS monte calro simulation. Figure 8.4 shows the inefficiency due to photo–nuclear interaction and electro-magnetic interaction for the lead/scintillator.[8]

In order to compare the inefficiency due to photo–nuclear interaction and the inefficiency due to sampling effect, we ran a monte calro simulation with the incident energy of 1.5 GeV for the lead/sicntillator, and obtained :

$$\text{Inefficiency(sampling effect)} = (1.7 \pm 0.4) \times 10^{-7}.$$

The punch through effect can be reduced by making the detector thicker. In order to reduce the punch through effect to 1×10^{-7} at GeV region, the detector length, L, has to be,

$$\begin{aligned} \text{Inefficiency(punch through)} &= e^{-\frac{L}{\frac{9}{7} \cdot X_0}} < 10^{-7} \\ &\Rightarrow L > 20.7 \cdot X_0, \end{aligned} \tag{8.2}$$

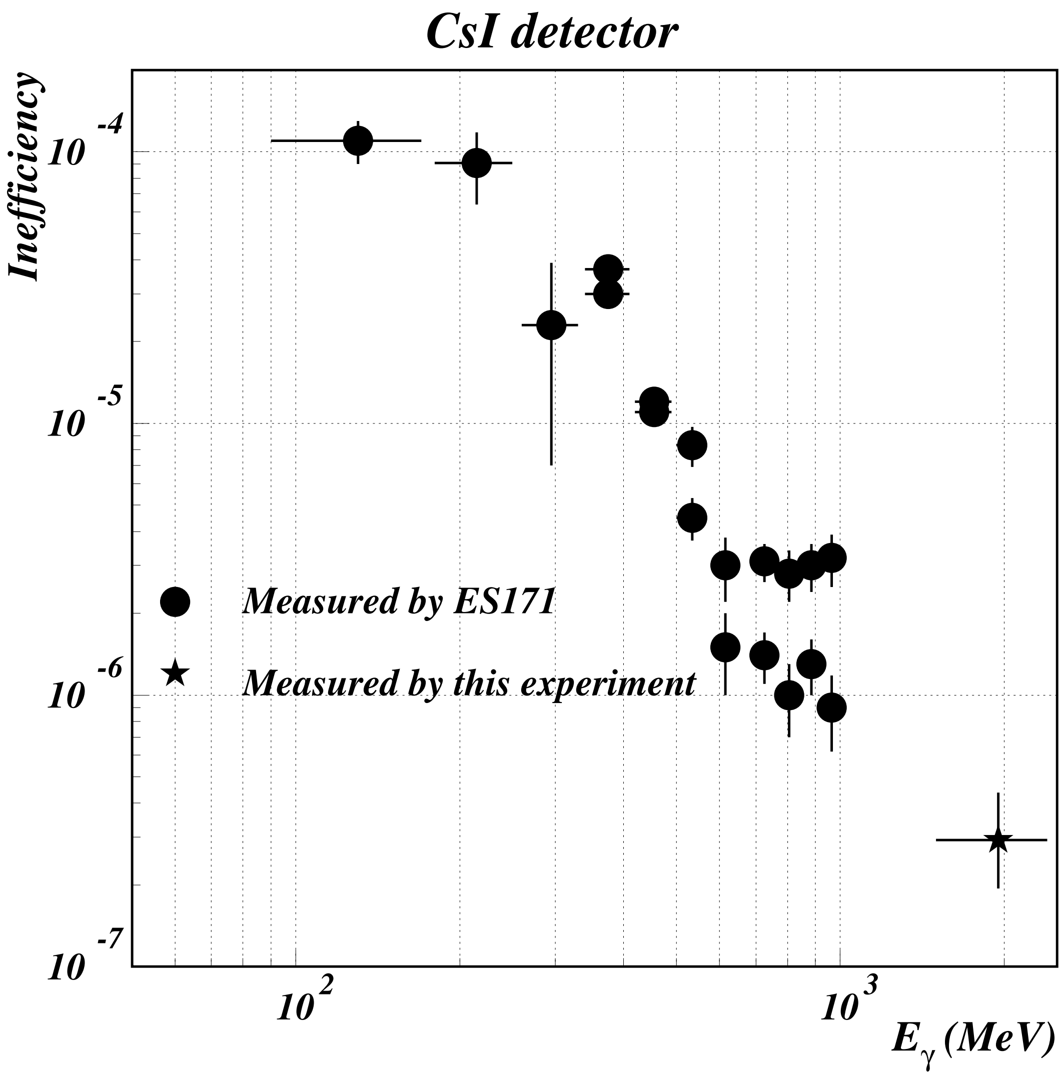

Figure 8.2: The inefficiency due to photo–nuclear interaction for the CsI detector is shown as a fraction of the incident photon energy. The solid line shows the inefficiency measured by ES171 experiment.[10] The star point shows the inefficiency measured by this experiment.

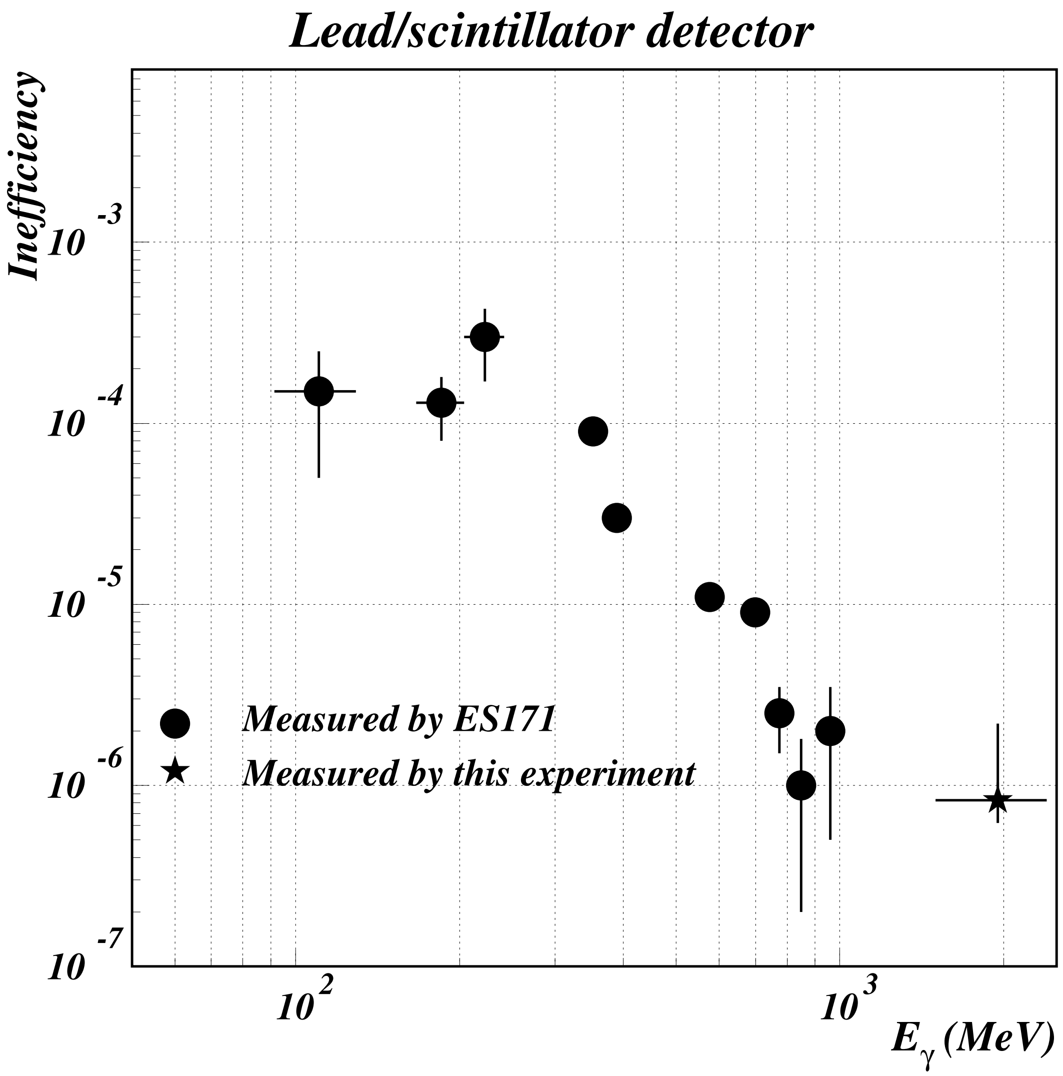

Figure 8.3: The inefficiency due to photo–nuclear interaction for the lead/scintillator is shown as a fraction of the incident photon energy. The solid line shows the inefficiency measured by ES171 experiment. [11] The star point shows the inefficiency measured by this experiment.

where X_0 is a radiation length.

Therefore, we can say the inefficiency due to electoro-magnetic interaction is 5 times smaller than the inefficiency due to photo–nuclear interaction for the lead/scintillator at 1.5 GeV. We can also say that the photo–nuclear interaction is still dominant source of the inefficiency at $1.5 < E_\gamma < 2.4$ GeV.

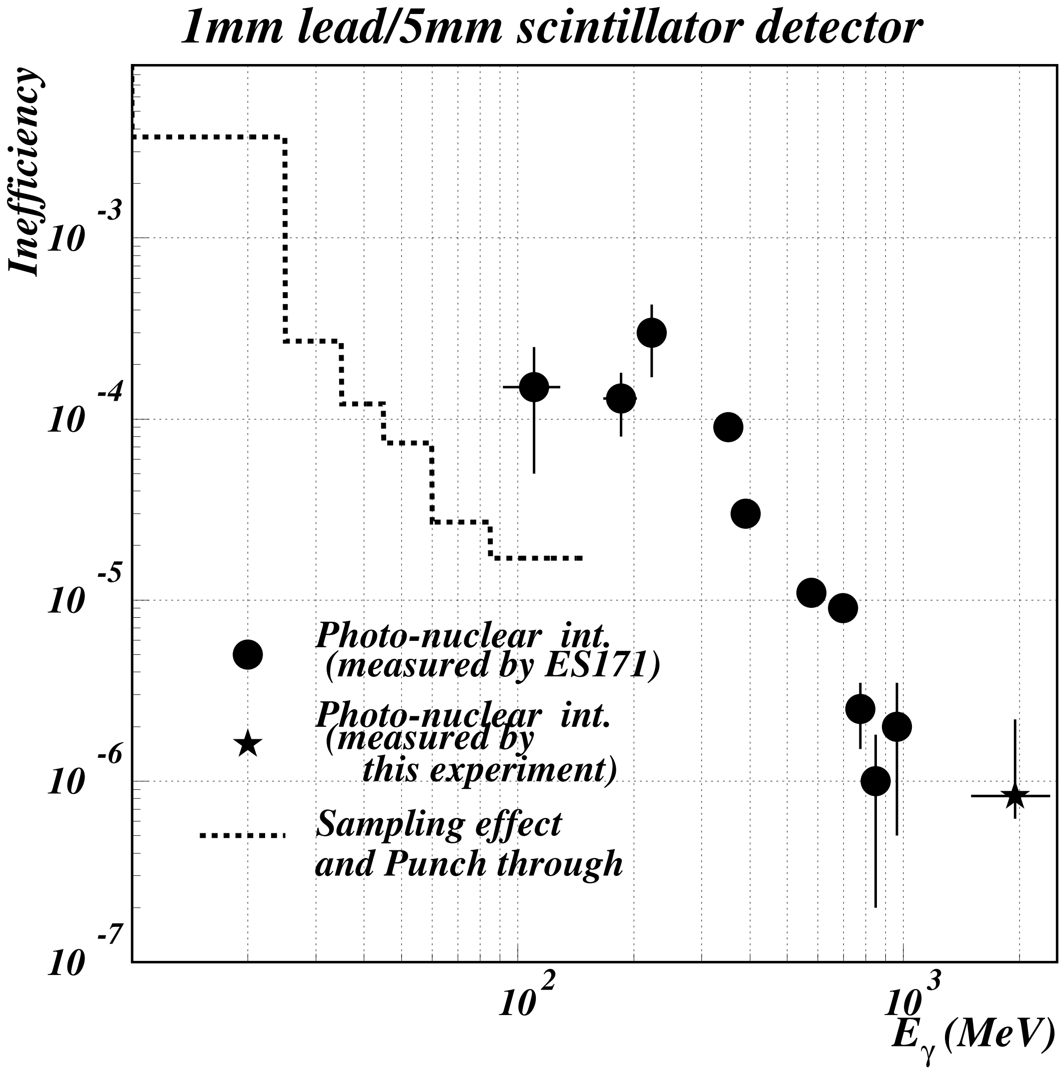

Figure 8.4: The inefficiecny due to photo–nuclear interaction for the lead/scintillator is shown as a fraction of the incident photon energy. The solid line was measured by ES171 experiment[11], and the star point was measured by this experiment. In addition, the sampling effect and the punch through effect are shown in this plot by a dashed line. The total length of the lead/scintillator is 18.2 X_0 at ES171 experiment.

8.5 Examination of $K_L \to \pi^0 \nu \bar{\nu}$ experiment

In this section, we discuss the inefficiency of the photon detector in the $K_L \to \pi^0 \nu \bar{\nu}$ experiment.

At KEK (High Energy Acceletator Research Organization in Janan), E391a is planning to search the $K_L \to \pi^0 \nu \bar{\nu}$ decay with using a hermetic photon veto surrounding the decay region. They are planning to measure only photon's energy and hit position.

In the future, this experiment will move to JHF (Japan Hadron Facility). At JHF, we can generate K_L with $P_K \sim 10$ GeV/c from 50 GeV PS (Proton Synchrotron). In the $K_L \to \pi^0 \nu \bar{\nu}$ experiment at JHF, it is also planning to measure only photon's energy and hit position and measure extra photons using a hermetic photon veto such as the lead/scintillator.

We measured the inefficiency of the lead/scintillator at $1.5 < E_\gamma < 2.4$ GeV to be $(8.3 \pm 2.1) \times 10^{-7}$ with 10 MeV threshold. A bottom up study of $K_L \to \pi^0 \nu \bar{\nu}$ experiment was done in the reference [8]. In this study, they assumed the inefficiency as 3.0×10^{-6} at $1 \leq E_\gamma < 3$ GeV. When they used the lead/scintillator as the photon veto and 10 MeV threshold, the experiment can be running with S/N ratio ~ 3 in the ideal model and S/N ~ 1 in the realistic model at $P_K = 10$ GeV/c.

Since the inefficiency of the lead/scintillator at this energy region is smaller than their assumption, we can say that the inefficiency is small enough to be used in the $K_L \to \pi^0 \nu \bar{\nu}$ experiment with $P_K \sim 10$ GeV/c.

Chapter 9

Conclusion

We measured the inefficiency due to photo–nuclear interaction for the CsI detector and the lead/scintillator detector. For photons with the energy, $1.5 < E_\gamma < 2.4$ GeV, the inefficiencies were $(2.93 \pm 0.89_{(stat.)}{}^{+1.15}_{-0.44}{}_{(sys.)}) \times 10^{-7}$ for CsI detector, and $(8.3 \pm 1.7_{(stat.)}{}^{+13.5}_{-1.2}{}_{(sys.)}) \times 10^{-7}$ for 1mm lead/5mm scintillator. The threshold is equivalent to 10 MeV incident photon energy.

We also considered the inefficiency of the lead/scintillator due to electro–magnetic interaction using EGS monte calro simulation and found that the inefficiency due to electro–magnetic interaction is 5 times smaller than the inefficiency due to photo–nuclear interaction at $E_\gamma \sim 1.5$ GeV.

These inefficiencies are small enough to be used in the $K_L \to \pi^0 \nu \bar{\nu}$ experiment with $P_K \sim 10$ GeV.

Appendix A

Inefficiency vs. *Etot* threshold

We also studied the inefficiency due to photo–nuclear interaction with several thresholds on *Etot*. We set the threshold to 1 MeV, 50 MeV and 100 MeV, and carried the out same analysis for each photon detector.

In section 6.1, we estimated the number of Mis-ID background events using two methods, but the number of background events estimated by the second method is always negligible. We believe the first method reflects the reality better, and used the first method to estimate the number of Mis-ID background events.

In the following sections, we describe the result of the inefficiency due to photo–nuclear interaction for different thresholds.

A.1 CsI Run

The number of incident photons and the acceptance for the photo–nuclear interaction are the same as 10 MeV threshold case. The number of the photo–nuclear interactions and the number of the Mis-ID backgroud events are summarized in Table A.1. Therefore, the inefficiencies due to photo–nuclear interaction are :

$$\begin{aligned}
\text{Inefficiency} &= (2.22 \pm 0.79_{(stat.)}{}^{+1.60}_{-0.34}{}_{(sys.)}) \times 10^{-7} \quad \text{(1 MeV threshold)}, \\
\text{Inefficiency} &= (5.00 \pm 1.18_{(stat.)}{}^{+3.56}_{-0.76}{}_{(sys.)}) \times 10^{-7} \quad \text{(50 MeV threshold)}, \\
\text{Inefficiency} &= (1.11 \pm 0.18_{(stat.)}{}^{+0.74}_{-0.17}{}_{(sys.)}) \times 10^{-6} \quad \text{(100 MeV threshold)},
\end{aligned}$$

where we estimated the systematic errors for the same three sources as for the 10 MeV threshold case.

Figure A.1 shows the inefficiency due to photo–nuclear interaction as a function of the threshold on *Etot*. The inefficiency is smaller for lower threshold.

A.2 Lead/scintillator Run

For the lead/scintillator runs, we also carried out the same analysis for 3 additional thresholds. The number of the photo–nuclear interactions and the number of the Mis-ID backgroud events are summarized in Table A.2. The inefficiencies due to photo–nuclear interaction are :

$$\begin{aligned}
\text{Inefficiency} &= (2.0 \pm 0.8_{(stat.)}{}^{+3.2}_{-0.3}{}_{(sys.)}) \times 10^{-7} \quad \text{(1 MeV threshold)}, \\
\text{Inefficiency} &= (1.8 \pm 0.2_{(stat.)}{}^{+2.5}_{-0.3}{}_{(sys.)}) \times 10^{-6} \quad \text{(50 MeV threshold)}, \\
\text{Inefficiency} &= (4.7 \pm 0.4_{(stat.)}{}^{+5.4}_{-0.7}{}_{(sys.)}) \times 10^{-6} \quad \text{(100 MeV threshold)},
\end{aligned}$$

Table A.1: The number of the photo–nuclear interactions and the number of the Mis-ID background events with 1 MeV, 50 MeV and 100 MeV threshold for the CsI detector.

	The number of the photo–nuclear interactions	The number of the Mis-ID background events
1 MeV threshold	8	0
50 MeV threshold	19	1
100 MeV threshold	45	5

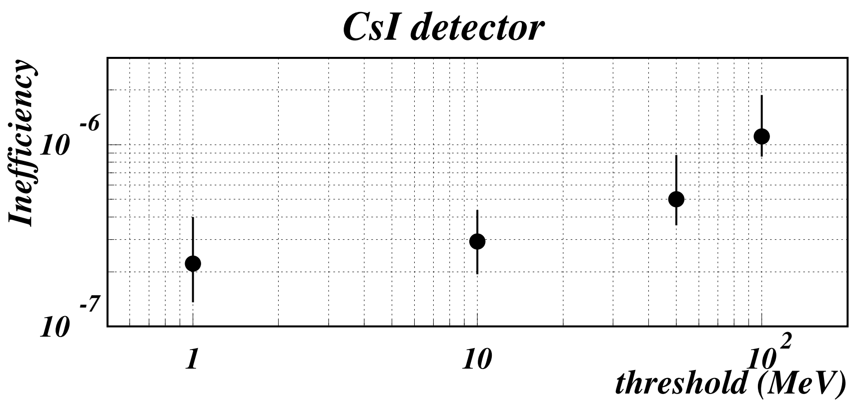

Figure A.1: The ineffiency of the CsI detector due to photo–nuclear interaction as a function of the threshold on *Etot*.

where we estimated the systematic error for the same three sources as for the 10 MeV threshold case.

Table A.2: The number of the photo–nuclear interactions and the number of the Mis-ID background events with 1 MeV, 50 MeV and 100 MeV threshold for the lead/scintillator detector.

	The number of the photo–nuclear interactions	The number of the Mis-ID background events
1 MeV threshold	6	0
50 MeV threshold	56	2
100 MeV threshold	148	6

Figure A.2 shows the inefficiency of due to photo–nuclear interaction as a function of the threshold on *Etot*. The inefficiency is smaller for lower thershold.

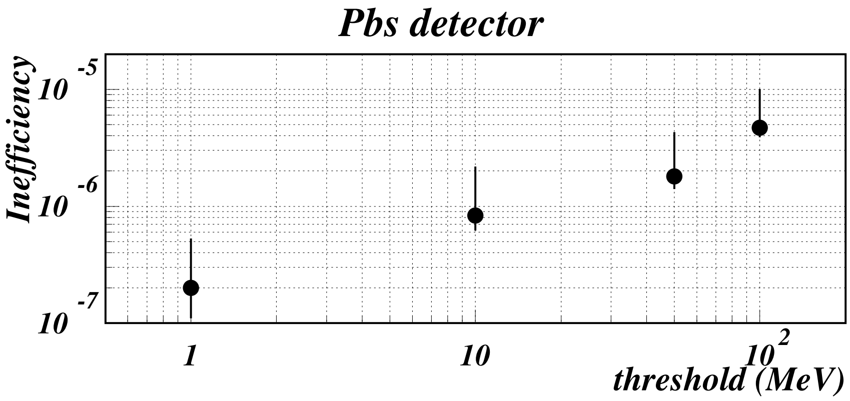

Figure A.2: The ineffiency of the lead/scintillator detector due to photo–nuclear interaction as a function of the threshold on *Etot*.

A.3 Summary

For each photon detector, the inefficiency due to photo–nuclear interaction decreases as the threshold is lowered, and reaches 10^{-7} level with 1 MeV threshold. This result will be useful when estimating the background level at a $K_L \to \pi^0 \nu \bar{\nu}$ experiment.

Bibliography

[1] J. Cronin, V. Fitch *et al.*, Phys. Rev. Lett. **13**, 138 (1964).

[2] M. Kobayashi and T. Maskawa, Prog. Theor. Phys. **49**, 652 (1973).

[3] L. Wolfenstein, Phys. Rev. Lett. **51**, 1945 (1983).

[4] A. Buras, Phys. Lett. **B333**, 476 (1994).

[5] G. Buchalla and A. Buras, Phys. Rev. **D54**, 6782 (1996).

[6] A. Alavi-Harati *et al.*, Phys. Rev. **D61**, 072006 (2000).

[7] T.Nakano *et al.*, Nucl. Phys. A **684**, 71 (2001).

[8] K.Manabe, Master Thesis, Osaka Univ., "Bottom Up Study of $K_L \to \pi^0 \nu \bar{\nu}$ experiment", (2000)

[9] K.H.Majer and J.Nitschke, Nucl. Instrum. Meth. **56**, 227 (1968)

[10] K.Mori, Master Thesis, Osaka Univ., "Measurement of inefficiency of photo–nuclear interaction with CsI photon counter", (1999).

[11] K.Kurebayashi, Master Thesis, Osaka Univ., "Measurement of inefficiency of photo–nuclear interaction with lead/scintillator sampling calorimater", (1999).

[12] T.Matsumura, Master Thesis, RCNP., "Measurement of the detection inefficiency for photons of energies 90 to 1000 MeV", (1999)